

2

NAVAL POSTGRADUATE SCHOOL Monterey, California

AD-A275 601



DTIC
ELECTRIC
FEB 16 1984
C

THESIS

DETERMINATION OF THE COMPLEX MASS
DENSITY OF AIR CONTAINED IN A RIGID
POROUS SOLID BY AN ACOUSTIC METHOD

by

Kevin A. Grundy

September, 1993

Thesis Co-Advisor:

S.R. Baker

Approved for public release; distribution is unlimited

DTIC QUALITY INSPECTED 2

94-05034



94 2 15 020

REPORT DOCUMENTATION PAGE				Form Approved OMB No 0704-0188	
1a REPORT SECURITY CLASSIFICATION UNCLASSIFIED			1b RESTRICTIVE MARKINGS		
2a SECURITY CLASSIFICATION AUTHORITY			3 DISTRIBUTION / AVAILABILITY OF REPORT		
2b DECLASSIFICATION / DOWNGRADING SCHEDULE			Approved for public release; distribution is unlimited.		
4 PERFORMING ORGANIZATION REPORT NUMBER(S)			5 MONITORING ORGANIZATION REPORT NUMBER(S)		
6a NAME OF PERFORMING ORGANIZATION Naval Postgraduate School		6b OFFICE SYMBOL (If applicable) 33	7a NAME OF MONITORING ORGANIZATION Naval Postgraduate School		
6c ADDRESS (City, State, and ZIP Code) Monterey, CA 93943-5000			7b ADDRESS (City, State, and ZIP Code) Monterey, CA 93943-5000		
8a NAME OF FUNDING / SPONSORING ORGANIZATION		8b OFFICE SYMBOL (If applicable)	9 PROCUREMENT INSTRUMENT IDENTIFICATION NUMBER		
8c ADDRESS (City, State, and ZIP Code)			10 SOURCE OF FUNDING NUMBERS		
			PROGRAM ELEMENT NO	PROJECT NO	TASK NO
					WORK UNIT ACCESSION NO
11 TITLE (Include Security Classification) DETERMINATION OF THE COMPLEX MASS DENSITY OF AIR CONTAINED IN A RIGID POROUS SOLID BY AN ACOUSTIC METHOD					
12 PERSONAL AUTHOR(S) Grundy, Kevin A.					
13a TYPE OF REPORT Master's Thesis		13b TIME COVERED FROM _____ TO _____		14 DATE OF REPORT (Year, Month, Day) 1993 September	
				15 PAGE COUNT 76	
16 SUPPLEMENTARY NOTATION The views expressed in this thesis are those of the author and do not reflect the official policy or position of the Department of Defense or the U.S. Govt					
17 COSATI CODES			18 SUBJECT TERMS (Continue on reverse if necessary and identify by block number)		
FIELD	GROUP	SUB-GROUP	Rigid Porous Solid, Complex Effective Mass Density, Effective Fluid Mass Density, Flow Resistance		
19 ABSTRACT (Continue on reverse if necessary and identify by block number)					
<p>An acoustical method for determining the frequency dependent complex effective mass density $\bar{\rho}_{eff}$ of air contained in a rigid porous solid is investigated. An apparatus was designed and built which holds an air-filled porous solid sample within a cylindrical tube capped on each end by identical moving-coil loudspeakers. A quantity of air is made to oscillate back and forth as a plug through the porous solid sample. $\bar{\rho}_{eff}$ is obtained from pressure and acceleration measurements taken at the ends of the sample tube. A description of the apparatus and the experimental results are presented.</p>					
20 DISTRIBUTION / AVAILABILITY OF ABSTRACT <input checked="" type="checkbox"/> UNCLASSIFIED/UNLIMITED <input type="checkbox"/> SAME AS RPT <input type="checkbox"/> DTIC USERS			21 ABSTRACT SECURITY CLASSIFICATION UNCLASSIFIED		
22a NAME OF RESPONSIBLE INDIVIDUAL Prof. S.R. Baker			22b TELEPHONE (Include Area Code) (408) 656-2732		22c OFFICE SYMBOL PH/Ba

Approved for public release; distribution is unlimited.

**Determination of the Complex Mass Density of Air
Contained in a Rigid Porous Solid by an Acoustic Method**

by

Kevin A. Grundy
Lieutenant, United States Navy
B.S., University of Idaho

Submitted in partial fulfillment
of the requirements for the degree of

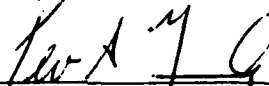
MASTER OF SCIENCE IN ENGINEERING ACOUSTICS

from the

NAVAL POSTGRADUATE SCHOOL

September 1993

Author:



Kevin A. Grundy

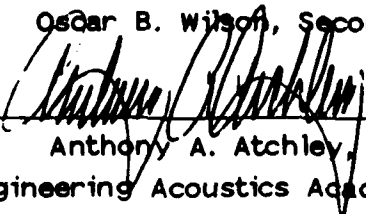
Approved by:



Steven R. Baker, Thesis Advisor



Oscar B. Wilson, Second Reader



Anthony A. Atchley, Chairman
Engineering Acoustics Academic Committee

ABSTRACT

An acoustical method for determining the frequency dependent complex effective mass density $\tilde{\rho}_{eff}$ of air contained in a rigid porous solid is investigated. An apparatus was designed and built which holds an air-filled porous solid sample within a cylindrical tube capped on each end by identical moving-coil loudspeakers. A quantity of air is made to oscillate back and forth as a plug through the porous solid sample. $\tilde{\rho}_{eff}$ is obtained from pressure and acceleration measurements taken at the ends of the sample tube. A description of the apparatus and the experimental results are presented.

Accession For		
NTIS	CRA&I	<input checked="" type="checkbox"/>
DTIC	TAB	<input type="checkbox"/>
Unannounced		<input type="checkbox"/>
Justification		
By		
Distribution /		
Availability Codes		
Dist	Avail and/or Special	
A-1		

TABLE OF CONTENTS

I.	INTRODUCTION	1
A.	BACKGROUND	1
B.	OBJECTIVES	2
II.	THEORY	3
A.	COMPLEX EFFECTIVE MASS DENSITY	3
B.	EXPERIMENTAL METHOD	5
III.	DESCRIPTION OF EXPERIMENT	8
A.	APPARATUS	8
1.	Speaker End Caps	9
2.	Sample Tube	9
3.	Sensor Calibration Procedures	10
a.	Accelerometer Calibration	11
b.	Pressure Sensor Calibration	16
(1)	Comparison Calibration	17
(2)	Calibration by Pistonphone	20
B.	EQUIPMENT SETUP	22
IV.	EMPTY TUBE EXPERIMENTS	25
A.	INITIAL EMPTY TUBE EXPERIMENT - THEORY	25
1.	Finite Wavelength Correction Factor	27
2.	Acceleration Correction Factor	29
B.	INITIAL EMPTY TUBE EXPERIMENT - RESULTS	31
C.	MODIFICATIONS TO APPARATUS	34

D.	REVISED EMPTY TUBE EXPERIMENT - THEORY	34
1.	Revised Finite Wavelength Correction Factor	36
E.	REVISED EMPTY TUBE EXPERIMENT - RESULTS	38
V.	POROUS SOLID SAMPLE EXPERIMENTS	41
A.	POROUS SOLID SAMPLE SELECTION	41
B.	THEORY	42
1.	Modified Acceleration Correction Factor	44
a.	Porosity Measurements	45
2.	Estimating k_L in a Rigid Porus Solid	46
C.	RESULTS	47
D.	INTERPRETATION OF RESULTS	52
1.	Calculation of β_{eff} using Biot's Theory	52
2.	Effective Fluid Mass Density	55
3.	Flow Resistance	57
VI.	CONCLUSIONS AND RECOMMENDATIONS	61
APPENDIX	A - EMPTY TUBE PROGRAM	62
APPENDIX	B - REVISED EMPTY TUBE PROGRAM	64
APPENDIX	C - POROUS SOLID SAMPLE PROGRAM	66
REFERENCES	68
INITIAL DISTRIBUTION LIST	69

ACKNOWLEDGEMENTS

I would like to thank Professor Baker for his patience and encouragement. I also wish to thank him for introducing me to this fascinating area of underwater acoustics. Most of all though I thank my wife Jeanne for her love and support, and Sophie for her constant companionship.

I. INTRODUCTION

A. BACKGROUND

In the past most of the interest in ocean acoustics focused on open ocean acoustics where the ocean depth can be considered infinite, and hence interactions with the bottom not significant. However, there has been a recent shift in interest to shallow water acoustics which has in turn increased the interest in bottom interactions since they are so common in shallow water. Like the sea surface, the bottom is an effective reflector and scatterer of sound and acts to redistribute in the ocean above it a portion of the sound incident upon it (Urlick, 1983, p.271).

The ocean bottom can be modeled as a fluid-filled porous solid and hence general research into the acoustic properties of porous media is of interest. Specifically, the solid-fluid interaction in a fluid-filled porous solid can provide insight into bottom interactions.

One way to characterize the microscopic solid-fluid interaction in a fluid-filled porous solid is through the use of the concept of complex effective mass density. It can be related to other familiar terms used in porous media acoustics, such as complex, or dynamic, tortuosity. In addition, other terms important in porous media research can be obtained from the complex effective mass density, such as effective fluid mass density and flow resistance.

B. OBJECTIVES

The objective of this research is to experimentally determine the complex effective mass density of air in a rigid porous solid over the frequency band of 10 to 1000 Hz. The experimental method being investigated involves using acoustic pressure and acceleration measurements to obtain the desired results. The theory is based on Newton's second law for a viscous fluid contained in a rigid porous solid.

II. THEORY

A. COMPLEX EFFECTIVE MASS DENSITY

Newton's second law for a fluid, ignoring all sources of dissipation except shear viscosity, is:

$$\rho \frac{\partial \vec{u}}{\partial t} + \rho(\vec{u} \cdot \nabla) \vec{u} = -\nabla p + \eta \nabla \times \nabla \times \vec{u}, \quad (2.1)$$

where ρ is the fluid mass density, \vec{u} is the fluid particle velocity, p is the fluid pressure, and η is the fluid shear viscosity. For small displacements, such as occur during the propagation of a low-amplitude sound wave, the quadratic terms in Equation (2.1) can be neglected, resulting in the linear differential equation

$$\rho \frac{\partial \vec{u}}{\partial t} = -\nabla p + \eta \nabla \times \nabla \times \vec{u}. \quad (2.2)$$

The corresponding linearized equation for a fluid-saturated rigid and stationary porous solid in terms of the average fluid velocity, $\langle \vec{u} \rangle$, is (Baker, 1986, pp. 334-335):

$$\rho_{eff} \frac{\partial \langle \vec{u} \rangle}{\partial t} = -\nabla \langle p \rangle - R_{flow} \langle \vec{u} \rangle, \quad (2.3)$$

where $\langle p \rangle$ is the average fluid pressure, ρ_{eff} is the effective fluid mass

density and R_{flow} is the flow resistance. ρ_{eff} and R_{flow} are operationally defined by:

$$\frac{1}{2} \rho_{eff} \langle \vec{u} \rangle^2 = \text{kinetic energy per unit fluid volume,}$$

$$R_{flow} \langle \vec{u} \rangle^2 = \text{rate of dissipation of fluid kinetic energy density.}$$

in addition, ρ_{eff} is always equal to or greater than the bulk fluid mass density, owing to the tortuosity of the pore geometry and to the nonuniformity of the microscopic velocity distribution across a pore.

Equation (2.3) can be written as:

$$\rho_{eff} \frac{\partial \langle \vec{u} \rangle}{\partial t} + R_{flow} \langle \vec{u} \rangle = -\nabla \langle p \rangle, \quad (2.4)$$

or, assuming a time harmonic solution of the form $e^{j\omega t}$, as:

$$\left[\rho_{eff} + \frac{R_{flow}}{j\omega} \right] \frac{\partial \langle \vec{u} \rangle}{\partial t} = -\nabla \langle p \rangle. \quad (2.5)$$

Equation (2.5) can now be written in terms of the average fluid acceleration, $\langle \vec{a} \rangle$:

$$\tilde{\rho}_{eff} \langle \vec{a} \rangle = -\nabla \langle p \rangle \quad (2.6)$$

where,

$$\tilde{\rho}_{eff} = \rho_{eff} + \frac{R_{flow}}{j\omega}. \quad (2.7)$$

is the complex effective mass density, the quantity of interest.

It is assumed that all quantities being measured have been averaged over the microscopic pore geometry of the porous solid, and since this research is only concerned with macroscopic physical quantities, the brackets indicating such quantities will henceforth be omitted.

B. EXPERIMENTAL METHOD

An experiment was designed and conducted in which a quantity of air is made to oscillate back and forth as a plug through a porous solid sample such that the pressure is zero at the midplane of the sample and equal in magnitude but opposite in phase at the ends. Figure 1 shows the setup used for the experiment.

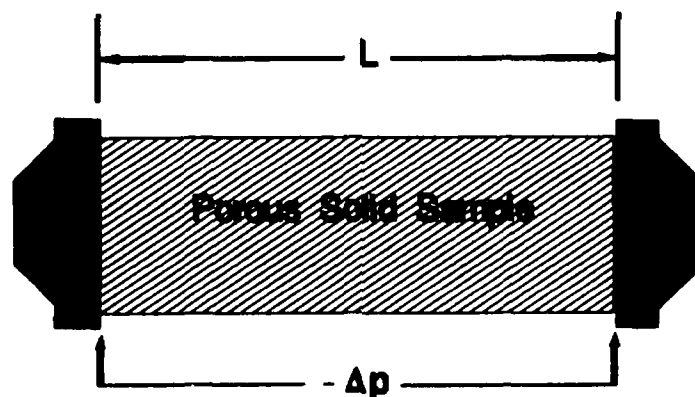


Figure 1 Experimental setup.

The complex mass density of the air can be obtained from pressure and acceleration measurements taken at the ends of the sample as follows.

If it assumed that the only motion is one-dimensional motion along the axis of the sample, Equation (2.6) can be rewritten as:

$$\bar{p}_{eff} = \frac{-\nabla p}{a} . \quad (2.8)$$

Because the air is oscillated at very low frequencies, the gradient in pressure along the sample can be approximated as the ratio of the pressure difference along the sample to the length of the sample,

$$\nabla p \approx \frac{p_R - p_L}{L} , \quad (2.9)$$

where p_R and p_L are the pressures at the right and left ends of the sample, respectively.

Equation (2.9) assumes that the wavelength of sound in air, λ , is much much greater than L . If this is not the case then a finite wavelength correction can be applied to Equation (2.9). Although, $\lambda \gg L$ at all frequencies in the experiments conducted, a finite wavelength correction was applied to improve the accuracy of the results. The finite wavelength correction factor for the empty tube experiments is discussed in Chapter IV and for the porous solid sample experiments in Chapter V.

Similarly, the acceleration of the air within the sample can be approximated as the average of the acceleration at the ends of the sample,

$$a \approx \frac{a_R + a_L}{2} , \quad (2.10)$$

where a_R and a_L are the acceleration at the right and left ends of the

sample, respectively.

Hence, using pressure and acceleration measurements taken at the ends of the sample the complex effective mass density of the air can be approximated by

$$\tilde{\rho}_{eff} = -\frac{2}{L} \frac{p_R - p_L}{a_R + a_L} . \quad (2.11)$$

III. DESCRIPTION OF EXPERIMENT

A. APPARATUS

The apparatus shown in Figure 2 was built to hold an air-filled porous solid sample. The apparatus holds the porous solid sample within a cylindrical sample tube which is capped on each end by a speaker end cap assembly (speaker end cap).

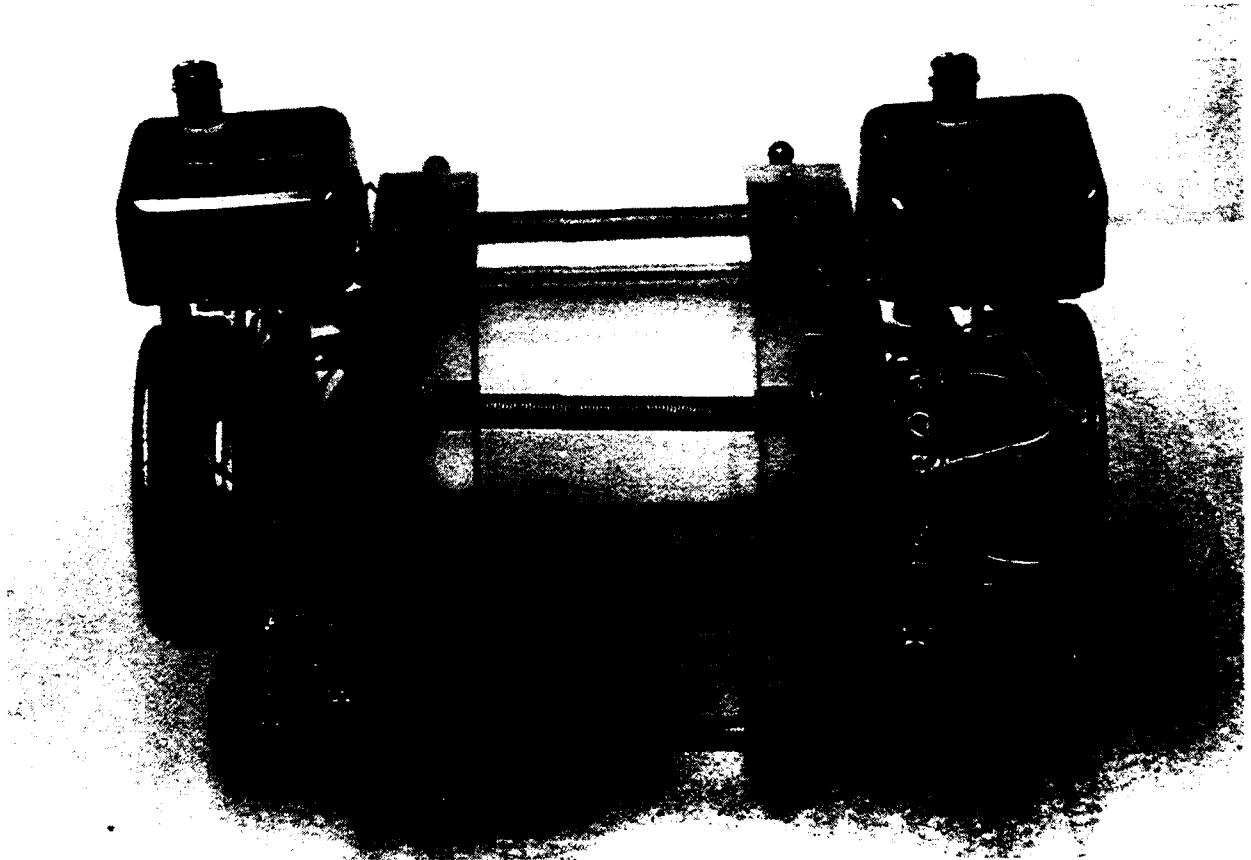


Figure 2 Apparatus used in complex mass density experiments.

1. Speaker End Caps

The speaker end caps, shown in Figure 3, consist of two identical moving-coil loudspeakers, each of which are attached to an acrylic mounting ring. The loudspeakers are four-inch diameter woofers manufactured by Radio Shack, Model 40-1022B (Tandy Corporation, Fort Worth, TX.). Modifications were made to each speaker end cap in order to take pressure and acceleration measurements.

To measure the pressure at each end of the sample, microphones were attached to the speaker end caps. The microphones are Radio Shack electret condenser microphones, Model 270-090, which were attached to two stainless steel wires positioned over the cone. In addition to supporting the microphone, the stainless steel wires also served as the electrical connections.

An accelerometer was attached to each speaker cone to measure acceleration at each end of the sample. An Endevco ISOTRONTM piezoelectric accelerometer, Model 25R, (Endevco Corporation, San Juan Capistrano, CA.) was selected for its extremely small size (approx 2 mm square) and weight (140 mg). The small dots on the surface of the each speaker cone were used in the accelerometer calibration procedure described below.

2. Sample Tube

A sample tube made of cast acrylic was chosen to hold the rigid porous solid sample. A sample tube 4.0 inches in length with an inner diameter of 3.5 inches and an outer diameter of 4.0 inches was selected. The length of the sample tube was chosen to minimize finite wavelength

effects throughout the entire frequency range of interest. The inner diameter of the tube was chosen to closely match the effective radiating diameter of the loudspeakers used in the speaker end caps.

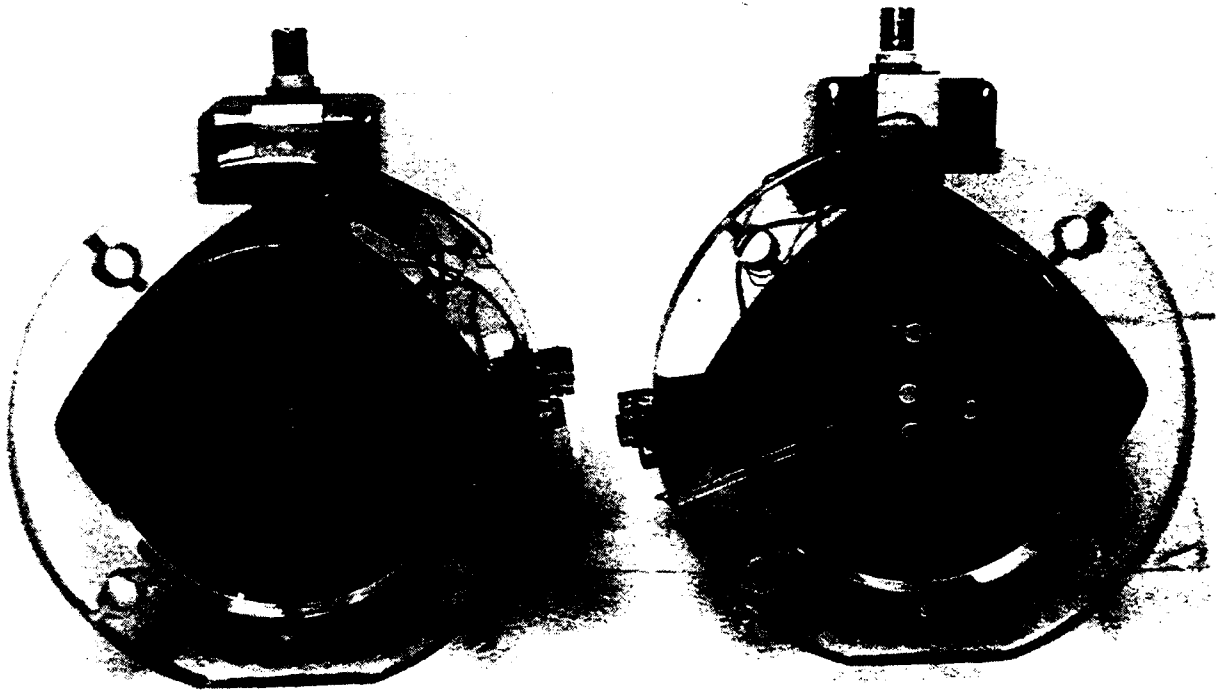


Figure 3 Speaker end cap assemblies.

3. Sensor Calibration Procedures

The accelerometers were calibrated by the manufacturer and a rated sensitivity was provided with each accelerometer. However, it was necessary to verify that the accelerometers were, in fact, measuring the acceleration of the air slug passing through the sample, and not just the acceleration at only one point on the speaker cone.

The condenser microphones selected as the "pressure sensors" were not calibrated by the manufacturer. Therefore it was necessary to calibrate them.

a. Accelerometer Calibration

As mentioned above, the accelerometers were calibrated by the manufacturer; therefore, a complete calibration was not necessary. It was, however, necessary to verify that the acceleration being measured was the same as the acceleration at any other point on the speaker cone. The idea was to compare the output of the accelerometers to another independent measure of acceleration.

It was not desirable to attach another device to the speaker end caps to provide the second independent measure of acceleration since the additional weight of the second device might affect the results. Instead, another option was chosen, which was to measure the velocity of the cone by a noncontact means using a laser doppler velocimeter and to compare the results to the acceleration as measured by the accelerometer.

The relationship between acceleration and velocity is given by

$$\frac{\partial u}{\partial t} = a, \quad (3.1)$$

where:

u = velocity,

a = acceleration.

In addition

$$u = A e^{j\omega t} \quad \text{and} \quad a = j\omega A e^{j\omega t}, \quad (3.2)$$

therefore

$$\frac{a}{u} = j\omega = j2\pi f. \quad (3.3)$$

Hence the ratio of acceleration to velocity is a linear function of frequency.

As mentioned above, the velocity of the speaker cone was measured using a laser vibrometer, a device which measures velocity by comparing the doppler shift in a light beam which has been reflected off the object whose velocity is desired. Therefore, the ratio of accelerometer output to vibrometer output should be a linear function of frequency.

Equation (3.3) above can be stated in terms of the outputs of the accelerometer and laser vibrometer as:

$$\frac{[\text{accelerometer voltage (mV)}][\text{accelerometer sensitivity (V/g)}]^{-1}[\text{gravity (m/s}^2\text{/g)}]}{[\text{vibrometer voltage (mV)}][\text{velocity range (m/s/V)}]} = 2\pi f,$$

or,

$$\frac{[\text{accelerometer voltage (mV)}]}{[\text{vibrometer voltage (mV)}]} = \frac{[\text{velocity range (m/s/V)}][\text{accelerometer sensitivity (V/g)}]}{[\text{gravity (m/s}^2\text{/g)}]} 2\pi f.$$

It can easily be seen this is an equation of a straight line when expressed in the form:

$$\frac{[\text{accelerometer voltage (mV)}]}{[\text{vibrometer voltage (mV)}]} = S_v 2\pi f.$$

Hence, if the ratio of accelerometer output voltage to laser vibrometer output voltage is plotted as a function of frequency, the curve should be as shown in Figure 4.

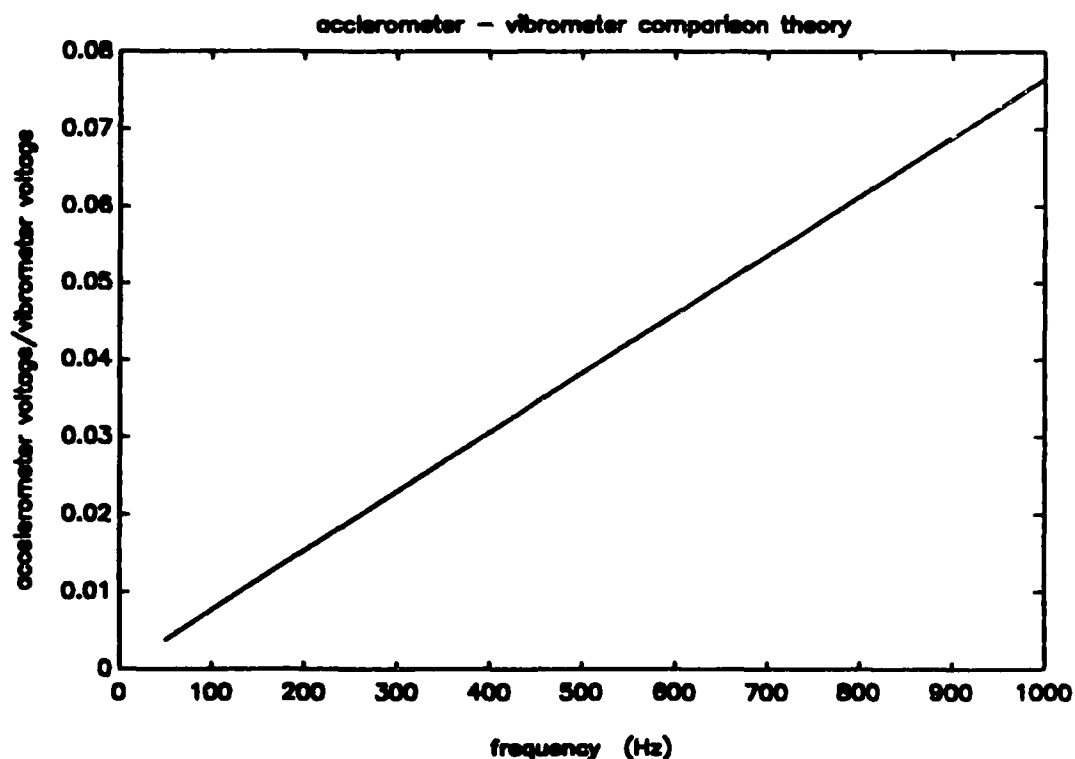


Figure 4 Theoretical comparison of accelerometer and vibrometer output.

One major benefit of using the laser vibrometer for measuring velocity is that it is capable of measuring the velocity at any point on the cone. Hence, if it could be shown that the ratio of accelerometer output to laser vibrometer output was a linear function of frequency, independent of the location on the speaker cone, the verification would be accomplished.

The setup shown in Figure 5 was used to verify that the accelerometers were, in fact, measuring the acceleration of the air slug passing through the sample, and not just the acceleration at only one point on the speaker cone.

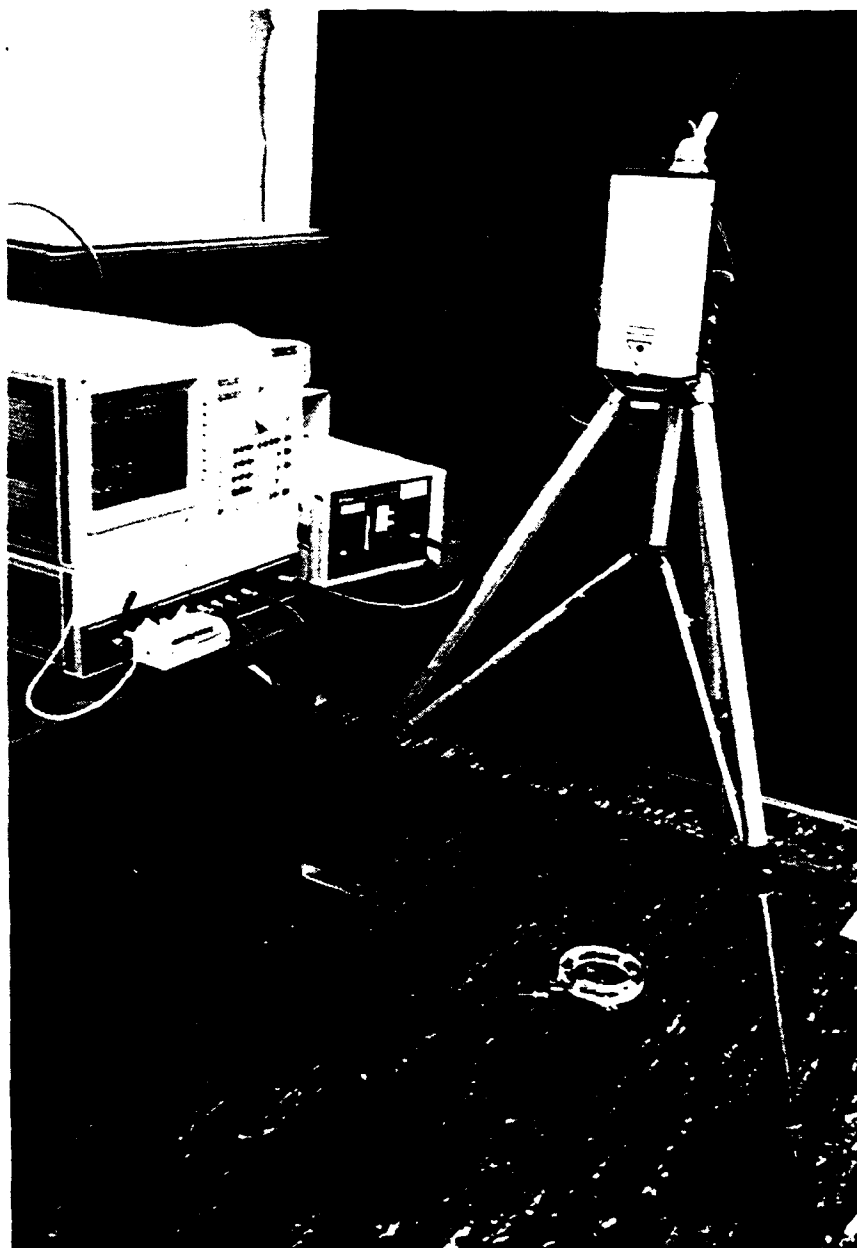


Figure 5 Accelerometer - vibrometer comparison setup.

Laser vibrometer output at several points on each speaker cone was compared to accelerometer output. Small dots of reflective material were placed on the surface of the speaker cone at each point to reflect the laser light beam.

The ratio of accelerometer output to laser vibrometer output for the right and left speaker end caps are shown in Figures 6 and 7, respectively. The theoretical lines were derived using a calibration factor of 25 mm/s/v for the laser doppler vibrometer and the individual accelerometer calibration constants supplied by the manufacturer. In both cases the ratio of accelerometer output to vibrometer output is essentially a linear function of frequency. The graphs shown are for a single comparison point on each speaker end cap; graphs for other points are similar.

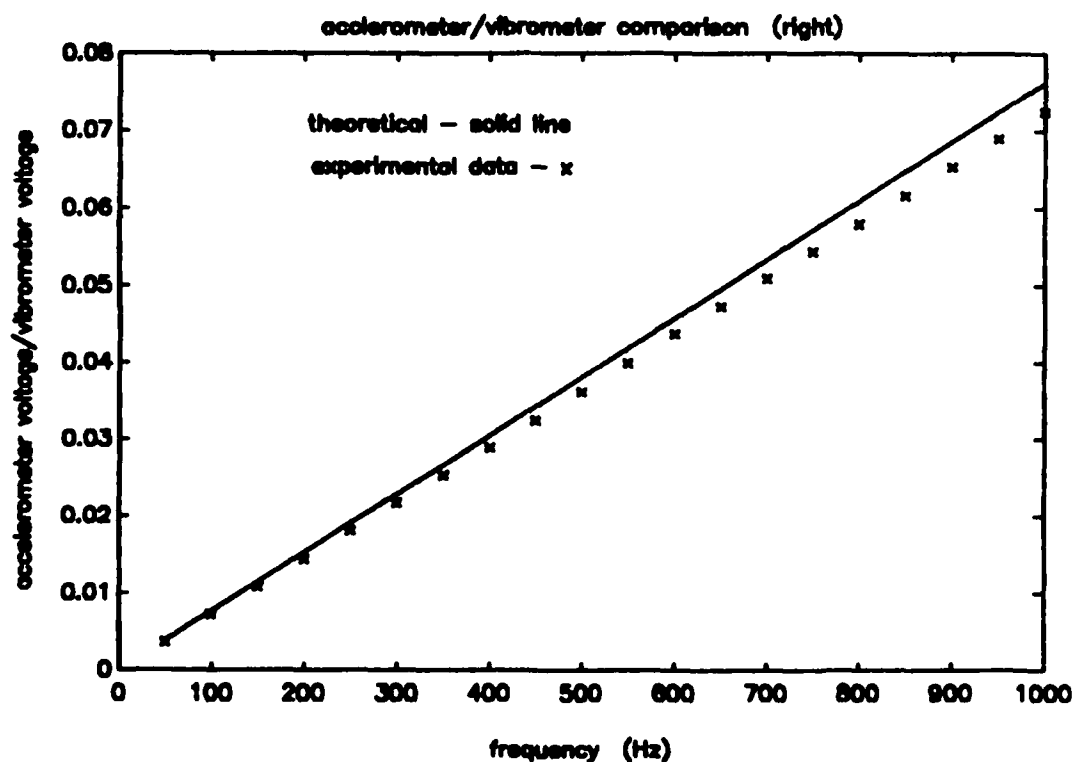


Figure 6 Ratio of accelerometer output to vibrometer output.

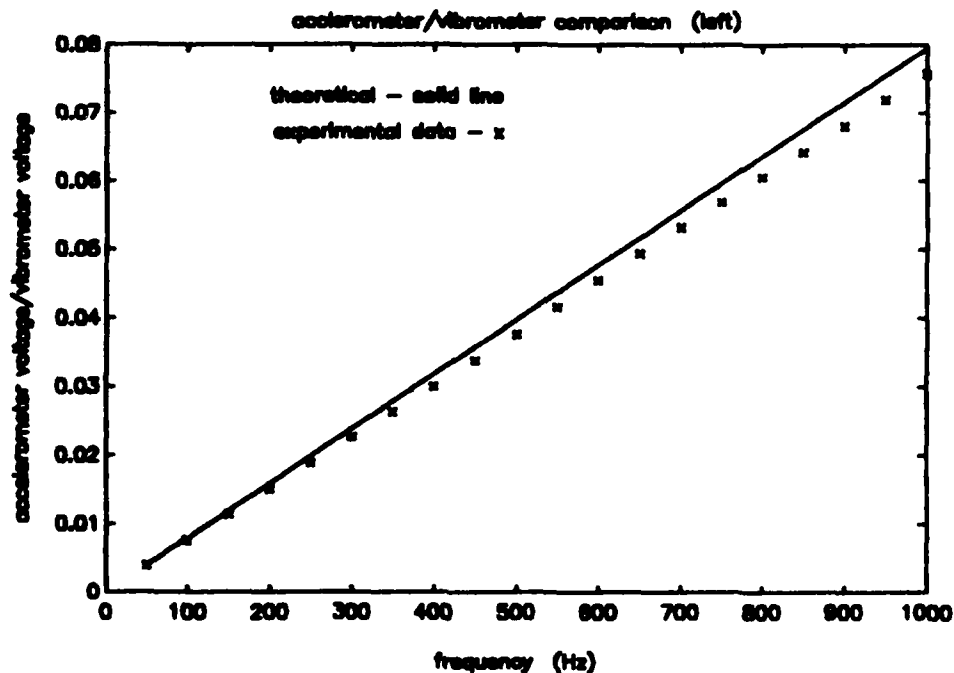


Figure 7 Ratio of accelerometer output to vibrometer output.

Since the ratio of accelerometer output to vibrometer output was found to be a linear function of frequency, independent of the location on the speaker cone, it is concluded that the output of the accelerometers is, in fact, a measure of the acceleration of the air slug passing through the sample.

b. Pressure Sensor Calibration

As previously mentioned, the condenser microphones selected as the "pressure sensors" were not calibrated by the manufacturer; therefore it was necessary to calibrate them prior to use. Two independent calibration methods were chosen, first, a comparison calibration, and second, with a pistonphone.

(1) *Comparison Calibration.* The condenser microphones were first calibrated using a comparison method. In this method, a comparison is made of the output of the condenser microphone to the output of a calibrated microphone while both are being subjected to the same sound field. Then, given the known sensitivity of the calibrated microphone in dB re 1v / Pa, the output of the calibrated microphone in dB re 1v / Pa, and the output of the condenser microphone in dB re 1v / Pa the sensitivity of the condenser microphone could be determined as follows:

$$\text{unknown sensitivity level} = \text{known sensitivity level} + \text{difference in output levels} \quad (3.4)$$

The setup shown in Figure 8 was used to accomplish the comparison. The moving-coil loudspeakers mounted in the speaker end caps were used to produce the sound field. A 1/8 inch diameter Bruel & Kjaer condenser microphone, Type 4138 (Bruel & Kjaer, Foster City, Ca.), with a sensitivity of - 68 dB re 1v / Pa (0.40 mV / Pa) was the calibrated microphone used for the comparison. A Hewlett-Packard Impedance Analyzer, Model 4194A (Hewlett-Packard Corporation, San Jose, Ca.), was used to measure and record the ratio of the output of the "pressure sensor" to the output of the B&K microphone, since it could do so while sweeping the drive signal to the loudspeakers over the desired frequency band, 10 to 1000 Hz.

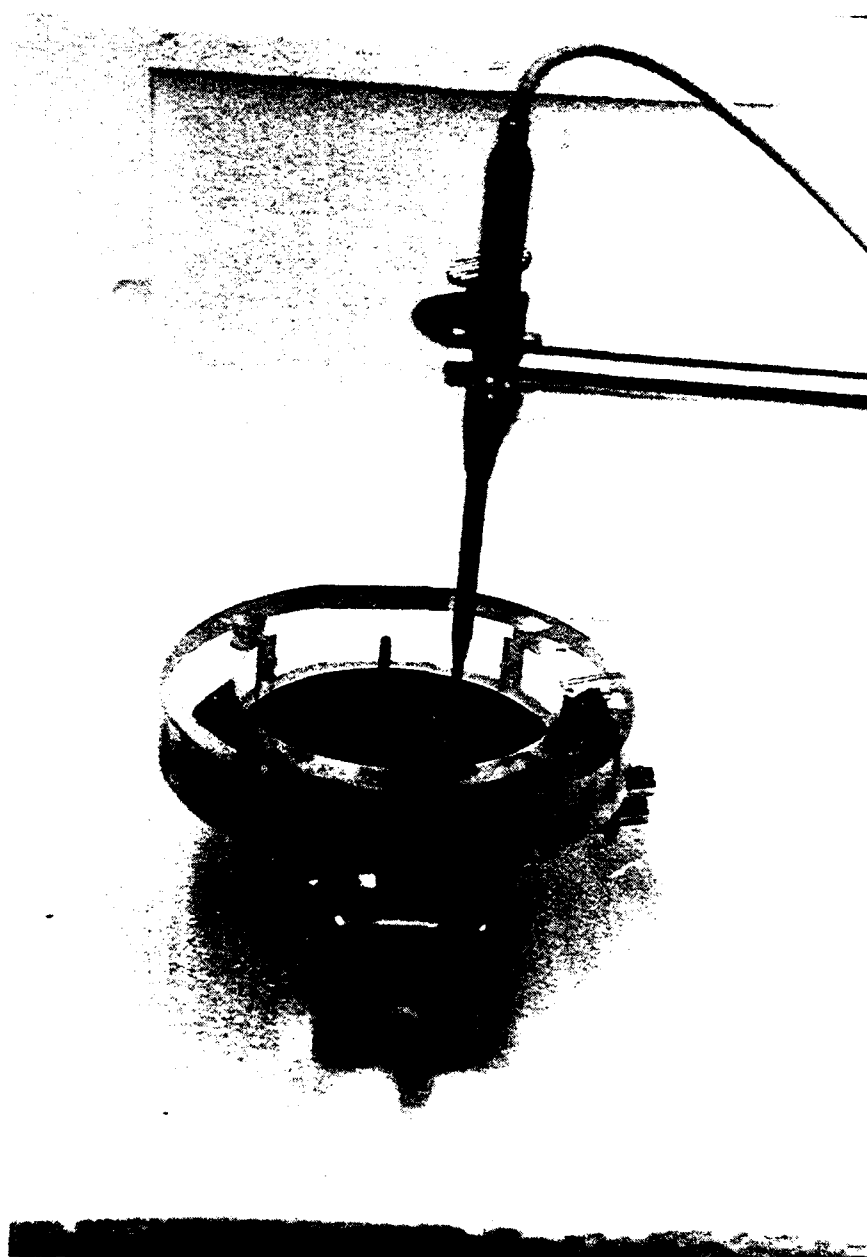


Figure 8 Comparison calibration setup.

As can be seen in Figures 9 and 10, the sensitivity of both "pressure sensors" was a function of frequency. A least squares fit of the data was used to determine this relationship with respect to frequency.

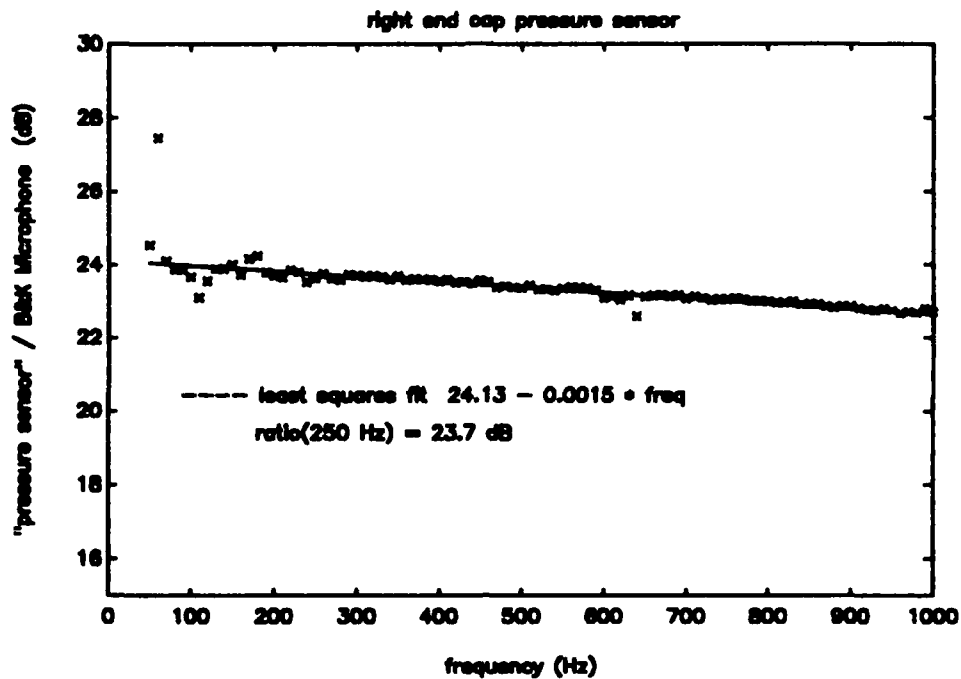


Figure 9 Ratio of "pressure sensor" output to B&K microphone output.

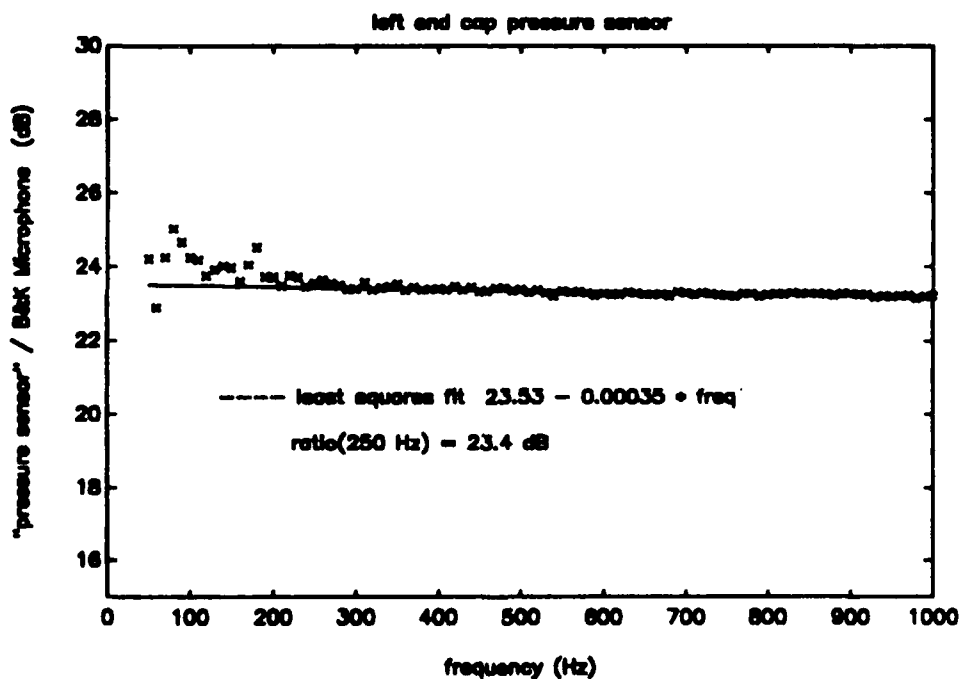


Figure 10 Ratio of "pressure sensor" output to B&K microphone output.

The resulting ratios of the output of the "pressure sensors" to the output of the B&K microphone were:

right pressure sensor / B&K = $24.1 - 0.0015 f$ dB,

left pressure sensor / B&K = $23.5 - 0.00035 f$ dB,

where f is frequency in Hz.

Given the above ratios and the sensitivity of the B&K microphone the unknown sensitivities were determined using Equation (3.4):

right pressure sensor sensitivity = $-43.9 - 0.0015 f$ dB re 1V / Pa,

left pressure sensor sensitivity = $-44.7 - 0.00035 f$ dB re 1V / Pa.

(2) *Calibration by Pistonphone.* The second method used to calibrate the "pressure sensors" was by pistonphone. A B&K Pistonphone, Model 4220, with a calibrated output of 123.9 dB re 20 μ Pa at 250 Hz was used. Had the frequency response of the "pressure sensors" been flat this method could have been used to verify the comparison calibration over the entire frequency band of interest. Unfortunately this was not the case; therefore, the pistonphone could only be used to verify the comparison calibration at 250 Hz.

The setup shown in Figure 11 was used. An adapter was needed since the pistonphone was designed to calibrate B&K microphones, which have a slightly smaller case than the Radio Shack condenser microphones being used.



Figure 11 Calibration by Pistonphone.

The sensitivities found using the B&K Pistonphone were:

right pressure sensor sensitivity = - 43.7 dB re 1V / Pa,

left pressure sensor sensitivity = - 44.6 dB re 1V / Pa.

At 250 Hz the sensitivities of the "pressure sensors" as found by the comparison calibration were:

right pressure sensor sensitivity = - 44.3 dB re 1V / Pa,

left pressure sensor sensitivity = - 44.7 dB re 1V / Pa.

These values are within 10% (1dB) of the sensitivities found using the B&K Pistonphone which would indicate the comparison calibration is valid, at least at 250 Hz.

B. EQUIPMENT SETUP

The equipment setup shown in Figure 12 was used for the experiments described below. The basic idea was to drive the moving-coil loudspeakers so that a null in pressure would be obtained at the center of the sample tube. Measurements of pressure and acceleration needed to be made at a set of frequencies chosen within the desired band of 10 to 1000 Hz.

In order to obtain a null at the center, it is necessary that the loudspeakers be driven out of phase. To prevent the phase from wandering, a method of locking the two phases together had to be found. The solution was to use two HP Function Generators, Model 3314, which were connected such that one was acting as a master and the second as a slave. The sync output of the master was connected to the trigger input of the slave. The major limitation to this setup was that it could only be used at 50 Hz and above due to limitations of the generators. Another minor limitation was that, because of their 50 ohm source impedance, the

HP 3314's could not provide a stable enough output voltage when loaded down by the loudspeakers. Therefore, the output of each HP 3314 was passed through an audio frequency amplifier, a Techron Model 7520 Power Supply Amplifier (Crown International, Inc., Elkhart, In.).

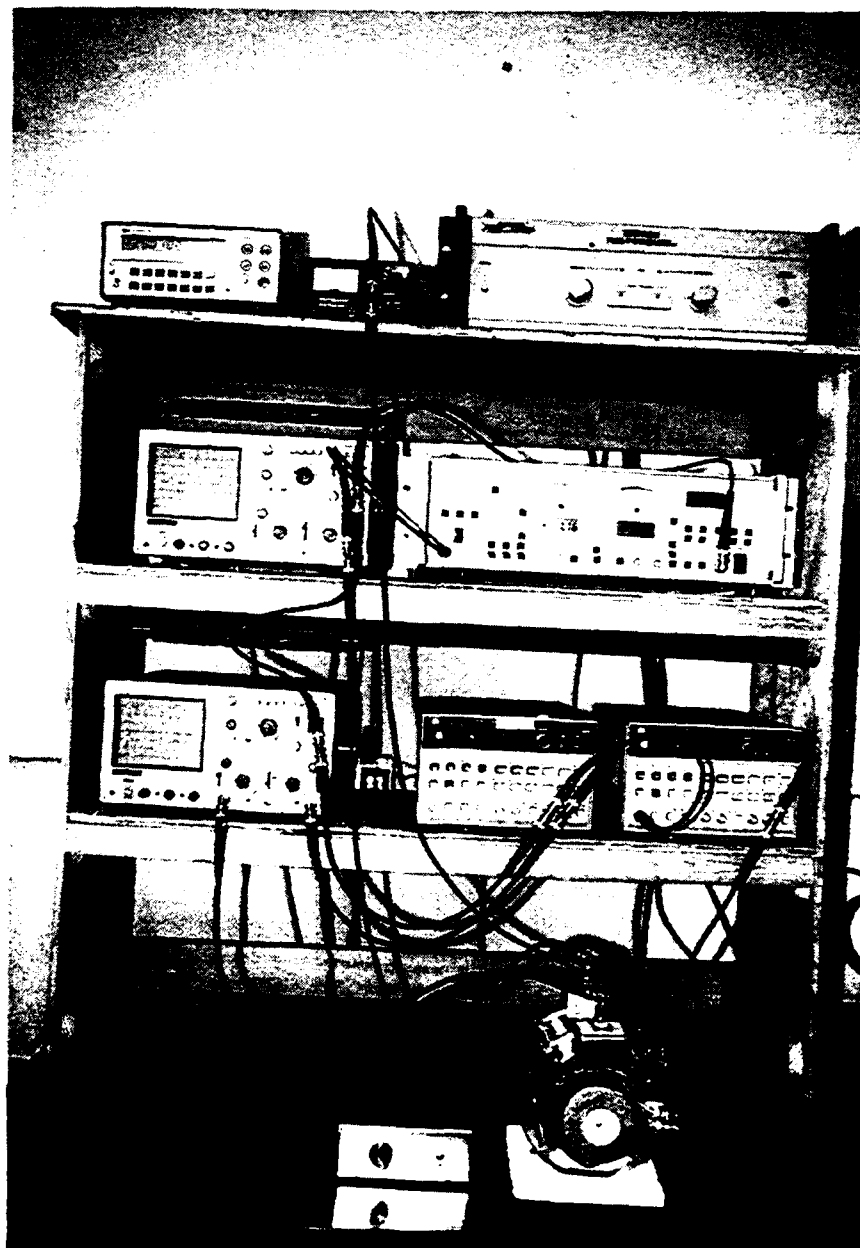


Figure 12 Equipment setup.

The output of each HP 3314 was monitored using a Kikusui Dual Channel Oscilloscope, Model DSS5020. This setup allowed the relationship between the phase of the two loudspeaker signals to be monitored on the same display.

Measurements were taken using a Stanford Research Systems Lock-in Amplifier, Model SR530 (Stanford Research Systems, Sunnyvale, Ca.). A lock-in amplifier was chosen since both magnitude and phase measurements needed to be taken. A second Kikusui Oscilloscope was used to monitor the signal being sent to the lock-in amplifier.

A connection box was designed and built to allow selection between each of the sensors. The output of the connection box was connected to the input of the lock-in amplifier and the oscilloscope.

All trigger inputs were connected to the sync output of the master HP 3314 for a single reference signal.

IV. EMPTY TUBE EXPERIMENTS

A. INITIAL EMPTY TUBE EXPERIMENT - THEORY

For the first experiment, an empty sample tube was used, as shown in Figure 13.

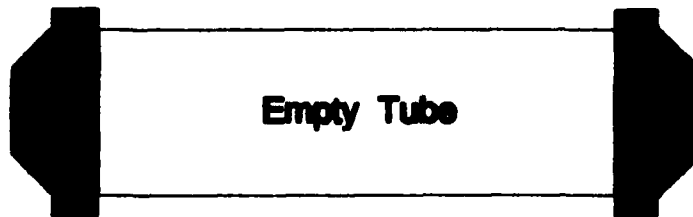


Figure 13 Empty tube experimental setup.

The objective of this experiment was to test the apparatus and equipment setup on a known quantity, namely air in an empty sample tube. The density of air at 20°C is 1.21 kg/m³ (KFCS, 1982, Appendix 10).

The complex effective mass density of the air contained in the empty sample tube, as defined in Chapter II, is the negative of the ratio of the gradient in pressure along the sample tube to the acceleration of the air within the sample tube, that is

$$\tilde{\rho}_{eff} = \frac{-\nabla p}{a} . \quad (4.1)$$

As previously discussed above, the gradient in pressure along the tube can be approximated as the ratio of the pressure difference along the sample tube to its length,

$$\nabla p = \frac{p_R - p_L}{L} = \overline{\nabla p}, \quad (4.2)$$

where p_R and p_L are the pressure at the right and left ends of the sample tube, respectively.

The acceleration of the air within the sample tube can be approximated as the average of the acceleration at each end of the sample tube,

$$a = \frac{a_R + a_L}{2} = \bar{a}. \quad (4.3)$$

where a_R and a_L are the acceleration at the right and left ends of the sample tube, respectively. Hence, Equation (4.1) can be written as

$$\bar{p}_{eff} = -\frac{2}{L} \frac{p_R - p_L}{a_R + a_L} = -\frac{\overline{\nabla p}}{\bar{a}}. \quad (4.4)$$

The calculation of \bar{p}_{eff} using Equations (4.2) through (4.4) appears to be rather simple; however, corrections need to be made to the above equations for the effects of sound propagation within the air column, and the slight difference in the cross-sectional area of the sample tube and the loudspeakers at either end. These corrections are discussed in the following subsections.

1. Finite Wavelength Correction Factor

Equation 4.2 assumes the air in the tube moves as a solid plug and as a result, that the pressure drop across the sample tube is distributed in a linear fashion as shown in Figure 14a. Unfortunately, plug flow is the limiting case when the wavelength of the oscillation of the air in the tube is infinite. For the cases of interest the wavelength is finite and the pressure drop is distributed approximately as shown in Figure 14b. (The pressure distribution shown in (b) is for a pressure wave with a wavelength of $2L$ and at one specific point in time.)

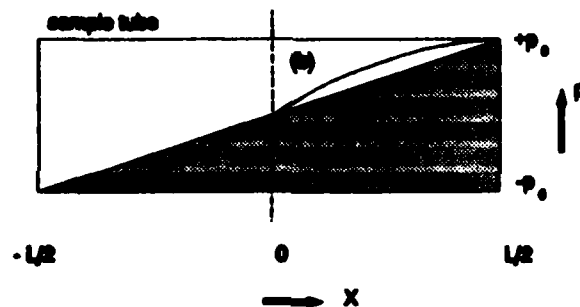


Figure 14 Pressure distribution within sample tube. (1) infinite wavelength, (2) finite wavelength.

The acoustic pressure and volume velocity at any point within the sample tube can be related using the concept of a velocity potential (ϕ). The following relationships exist among acoustic pressure (p), particle velocity (u), and velocity potential (ϕ) for plane wave propagation in one dimension (generalized to the case of porous media from Kinsler, et al., 1982, pp. 104-107):

$$p = -j \omega \bar{\rho}_{eff} \phi, \quad (4.5)$$

and

$$u = \frac{d\phi}{dx} . \quad (4.6)$$

For the finite wavelength case the pressure distribution is

$$p(x) = p_0 \sin kx , \quad (4.7)$$

where k is the wave number of the pressure wave, and hence

$$\overline{Vp} = \frac{2 p_0 \sin kL/2}{L} . \quad (4.8)$$

Substituting Equation (4.7) into Equation (4.5) and solving for ϕ yields

$$\phi(x) = - \frac{p_0 \sin kx}{j \omega \bar{p}_{eff}} . \quad (4.9)$$

Equation (4.6) then becomes

$$u(x) = - \frac{k p_0 \cos kx}{j \omega \bar{p}_{eff}} . \quad (4.10)$$

Therefore, the particle acceleration is

$$a(x) = - k \frac{p_0}{\bar{p}_{eff}} \cos kx , \quad (4.11)$$

and the acceleration of the air at each end of the sample tube is

$$a(\pm L/2) = - k \frac{p_0}{\bar{p}_{eff}} \cos kL/2 . \quad (4.12)$$

Therefore,

$$\bar{a} = -k \frac{P_0}{\bar{\rho}_{eff}} \cos kL/2 . \quad (4.13)$$

Equations (4.8) and (4.13) can be combined to yield

$$-\frac{\nabla p}{\bar{a}} = \bar{\rho}_{eff} \left[\frac{\tan kL/2}{kL/2} \right] . \quad (4.14)$$

Solving Equation (4.14) for the complex effective mass density then gives

$$\bar{\rho}_{eff} = -\frac{\nabla p}{\bar{a}} \cdot \frac{1}{f_{wcf}} , \quad (4.15)$$

where

$$f_{wcf} = \left[\frac{\tan kL/2}{kL/2} \right] \quad (4.16)$$

is the finite wavelength correction factor.

2. Acceleration Correction Factor

As previously stated, the acceleration of the air within the sample tube is taken to be the average of the acceleration at each end of the sample tube. However, the acceleration being measured is the acceleration of the speaker cones. Unfortunately, the acceleration of the speaker cones and the acceleration at the ends of the sample tube are not equal because the cross-sectional area of the sample tube and loudspeaker are not quite equal. However, the mass flow rate of the air at the surface of the

speaker cone is equal to the mass flow rate of air at the end of the sample tube. Hence,

$$a_{cone} A_{cone} = a_{tube} A_{tube} \quad (4.17)$$

where

a_{cone} = acceleration of the surface of the speaker cone,

a_{tube} = acceleration of the air at the end of the sample tube,

A_{cone} = cross-sectional area of the speaker cone,

A_{tube} = cross-sectional area of the end of the sample tube,

Solving Equation (4.17) for the desired quantity, a_{tube} , yields:

$$a_{tube} = a_{cone} \frac{A_{cone}}{A_{tube}} = a_{cone} \left[\frac{D_{cone}}{D_{tube}} \right]^2 \quad (4.18)$$

where

D_{cone} = diameter of the speaker cone (8.3 cm.),

D_{tube} = diameter of the sample tube (8.9 cm.).

Hence, Equation (4.3) can be written as:

$$a = \frac{a_R + a_L}{2} = \frac{a_{R_c} + a_{L_c}}{2} \cdot acf \quad (4.19)$$

where a_{R_c} and a_{L_c} are the acceleration of the right and left speaker cones, respectively, and

$$acf = \left[\frac{D_{cone}}{D_{tube}} \right]^2 = 0.870 \quad (4.20)$$

is the acceleration correction factor. Equation (4.15) then becomes

$$\tilde{p}_{eff} = - \frac{\overline{\nabla p}}{\frac{a_{R_t} + a_{L_t}}{2} \cdot acf} \cdot \frac{1}{f w c f} . \quad (4.21)$$

B. INITIAL EMPTY TUBE EXPERIMENT - RESULTS

Measurements were taken over the frequency range of 50 to 500 Hz in 10 Hz steps and over the frequency range of 500 to 1000 Hz in 50 Hz steps. At each frequency the amplitude and phase of the slave HP 3314 was adjusted to obtain a pressure null at the center of the sample tube. It was assumed when this condition was obtained that the two loudspeakers were moving exactly out of phase. Once the null was obtained, pressure and acceleration measurements were taken at each end using the SR Lock-in Amplifier. Both amplitude and phase measurements were taken since a complex quantity was being calculated.

A computer program was written to compute the complex effective mass density at each frequency using Equation (4.21). Then, since

$$\tilde{p}_{eff} = \rho_{eff} - j \frac{R_{flow}}{\omega} , \quad (4.22)$$

the effective fluid mass density is

$$\rho_{eff} = \text{Re}[\tilde{p}_{eff}] , \quad (4.23)$$

and the flow resistance is

$$R_{flow} = - \omega \text{Im}[\tilde{p}_{eff}] . \quad (4.24)$$

A copy of the program is attached as Appendix A.

Although the results, as shown in Figures 15 and 16, were initially encouraging, the steady increase in both the density and flow resistance at frequencies above 700 Hz was unexpected and thus warranted further investigation.

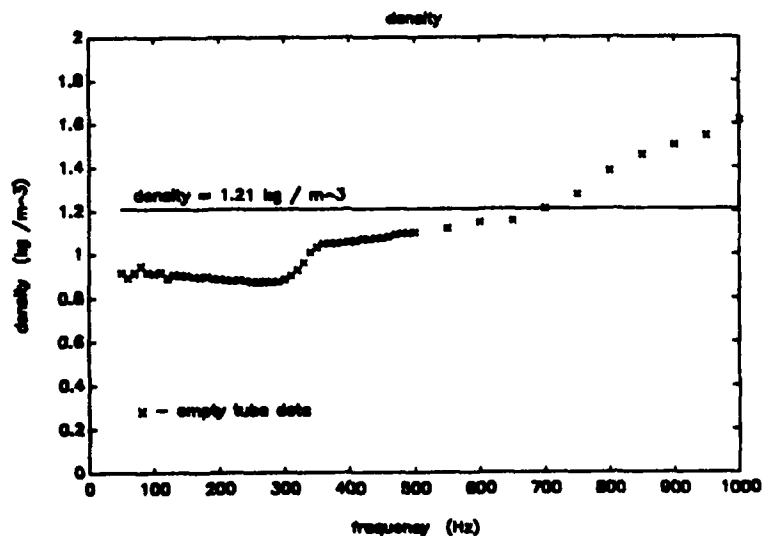


Figure 15 Initial empty tube results - effective fluid mass density.

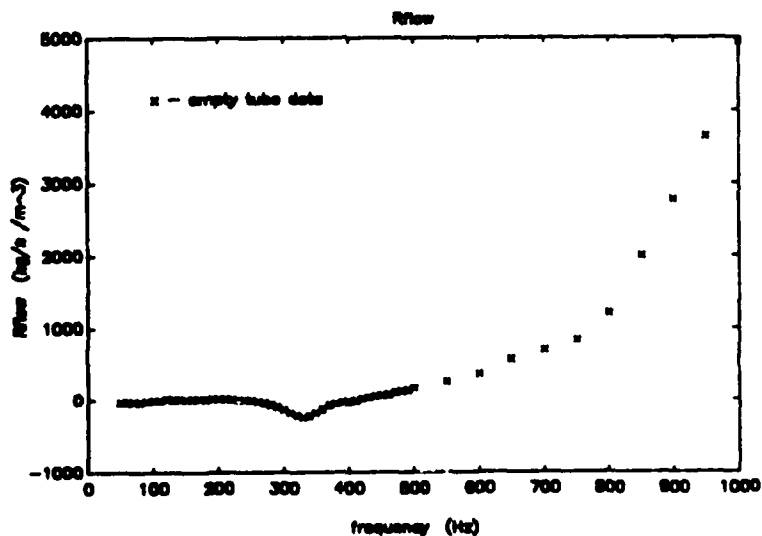


Figure 16 Initial empty tube results - flow resistance.

Careful examination of the data suggested a possible problem with the pressure phase measurements. Although the condenser microphones used as "pressure sensors" were calibrated with respect to pressure magnitude there was no calibration made with respect to pressure phase. A comparison with respect to pressure phase was made with the calibrated B&K microphone used to calibrate the sensors, since it has a flat phase response. The results, shown in Figure 17, indicate that this is a potential source of the problem.

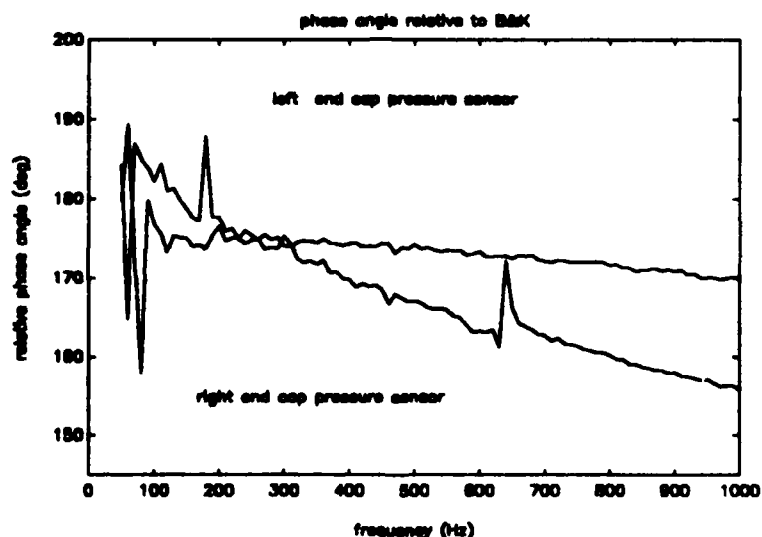


Figure 17 Pressure sensor comparison to B&K with respect to phase.

Attempts were made to correct for this problem; however, it was decided that since more accurate sensors were available, modifying the apparatus would be a simpler solution. In addition, a revised experimental procedure was developed to correct for another potential source of error due to air compression.

C. MODIFICATIONS TO APPARATUS

The left end cap pressure sensor was replaced with a PCB Piezotronics microphone, Model 103A (PCB Piezotronics, Inc., New York, NY). This microphone is rated to 25 psi with a sensitivity of 2080 mV/psi or 0.3017 mV/Pa and was supplied with a calibration curve good from 0 - 3 psi. The modification to the left speaker end cap changed the effective length of the sample to 92.4 mm vice 102 mm.

The center pressure sensor was also replaced with a PCB Piezotronics microphone, Model 103A, with a rated sensitivity of 1913 mV/psi or 0.2775 mV/Pa. The right end cap pressure sensor was not replaced for reasons which will become clear when the revised experimental procedure is discussed.

D. REVISED EMPTY TUBE EXPERIMENT - THEORY

The acceleration correction factor previously developed only corrected for the difference in the cross-sectional areas of speaker cone and the tube. There was however, another potential source of error that had not been considered, and that was the acceleration loss between the surface of the speaker cone and the end of the sample due to the compressibility of air. Hence, either an additional correction factor needed to be applied to Equation (4.21) to correct for that loss or the procedure needed to be revised to eliminate the loss. It was decided that the best approach was to revise the procedure to eliminate the loss.

Instead of adjusting the slave HP 3314 to obtain a null in pressure at the center of the sample tube, the slave HP 3314 was adjusted to obtain

a null at the right end of the sample tube. The resulting pressure drop across the sample is distributed as shown in Figure 18. The wavelength of the pressure wave is finite in all cases. (The pressure distribution shown is for a pressure wave with a wavelength of $4L$ and at one specific point in time.)

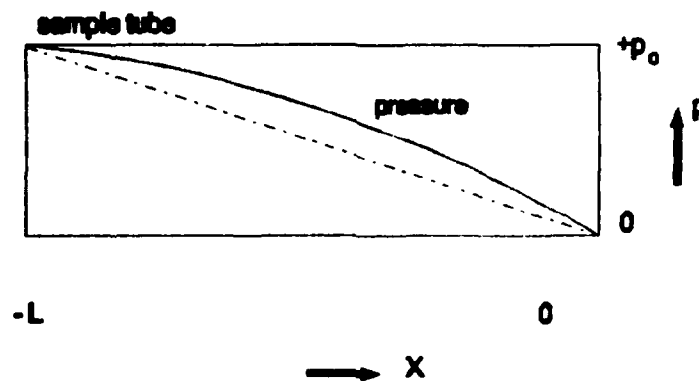


Figure 18 Pressure distribution within sample tube with pressure null at the right end of the sample.

As a result, acceleration loss between the surface of the speaker cone and the end of the sample due to the compressibility of air is identically zero (since the acoustic pressure there is zero) and the acceleration of the air within the sample tube is the acceleration at the right end of the sample tube. Therefore,

$$a = a_R = a_{R_s} \cdot acf. \quad (4.25)$$

The gradient in pressure along the sample tube can still be approximated as the ratio of the pressure difference along the sample tube to its length; however, since the pressure is zero at the right end of the sample the pressure difference along the sample is just the pressure at

the left end of the sample. Therefore, Equation (4.2) can be written as

$$\nabla p = \frac{-p_L}{L} = \overline{\nabla p} . \quad (4.26)$$

In addition to the changes listed above, the finite wavelength correction factor as defined by Equation (4.16) needed to be changed since the pressure drop across the sample tube was no longer distributed as shown in Figure 14.

1. Revised Finite Wavelength Correction Factor

As previously stated, the acoustic pressure and volume velocity at any point within the sample tube can be related using the following relationships for plane wave propagation in one dimension:

$$p = -j \omega \tilde{\rho}_{eff} \Phi , \quad (4.27)$$

and

$$u = \frac{d\Phi}{dx} . \quad (4.28)$$

For the case the shown in Figure 18, the pressure distribution is

$$p(x) = - p_0 \sin kx , \quad (4.29)$$

where k is the wave number of the pressure wave, and hence

$$\overline{\nabla p} = - \frac{p_0 \sin kL}{L} . \quad (4.30)$$

Substituting Equation (4.29) into Equation (4.27) and solving for ϕ yields

$$\phi(x) = \frac{p_0 \sin kx}{j \omega \bar{\rho}_{eff}} . \quad (4.31)$$

Equation (4.28) then becomes

$$u(x) = \frac{k p_0 \cos kx}{j \omega \bar{\rho}_{eff}} . \quad (4.32)$$

Therefore, the particle acceleration is

$$a(x) = k \frac{p_0}{\bar{\rho}_{eff}} \cos kx , \quad (4.33)$$

and the acceleration of the air at the right end of the sample tube is

$$a_R = a(0) = k \frac{p_0}{\bar{\rho}_{eff}} . \quad (4.34)$$

Therefore,

$$a_{R_1} \cdot acf = k \frac{p_0}{\bar{\rho}_{eff}} . \quad (4.35)$$

Equations (4.30) and (4.35) can be combined to yield

$$- \frac{\nabla p}{a_{R_1} \cdot acf} = \bar{\rho}_{eff} \left[\frac{\sin kL}{kL} \right] . \quad (4.36)$$

Solving Equation (4.36) for the complex effective mass density then gives

$$\bar{\rho}_{eff} = - \frac{\nabla p}{a_{R_1} \cdot acf} \cdot \frac{1}{f \omega c f} \quad (4.37)$$

where

$$fwcf = \left[\frac{\sin kL}{kL} \right] \quad (4.38)$$

is the revised finite wavelength correction factor.

E. REVISED EMPTY TUBE EXPERIMENT - RESULTS

Measurements were again taken over the frequency range of 50 to 500 Hz in 10 Hz steps and over the frequency range of 500 to 1000 Hz in 50 Hz steps. However, this time the amplitude and phase of the slave HP 3314 was adjusted at each step to obtain a null in pressure at the right end of the sample tube. Once the null was obtained, pressure and acceleration measurements (amplitude and phase) were taken at the left and right ends of the sample tube, respectively, using the SR Lock-in Amplifier.

A computer program was written to compute the complex effective mass density at each frequency using Equation (4.37). Then, since

$$\tilde{\rho}_{eff} = \rho_{eff} - j \frac{R_{flow}}{\omega}, \quad (4.22)$$

the effective fluid mass density is

$$\rho_{eff} = \text{Re}[\tilde{\rho}_{eff}], \quad (4.23)$$

and the flow resistance is

$$R_{flow} = -\omega \text{Im}[\tilde{\rho}_{eff}]. \quad (4.24)$$

A copy of the program is attached as Appendix B.

The revised empty tube results for effective fluid mass density and flow resistance are shown in Figures 19 and 20 respectively. The change in procedure had a dramatic effect on the effective fluid mass density above 700 Hz. It also had an effect on the flow resistance, but not so dramatic.

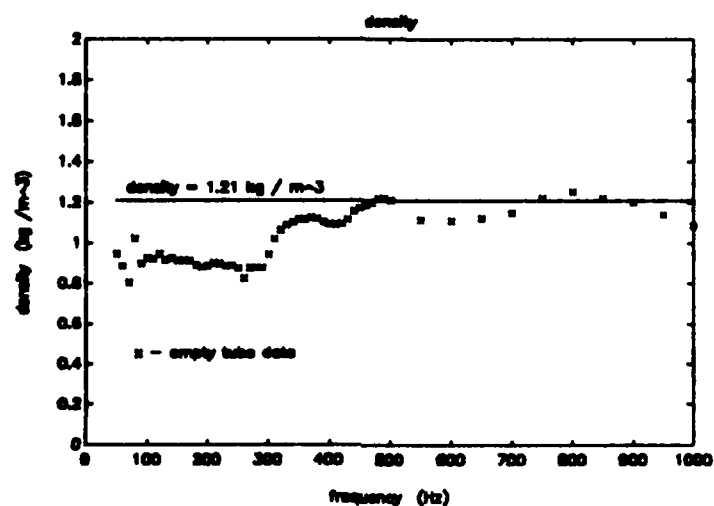


Figure 19 Revised empty tube results - effective fluid mass density.

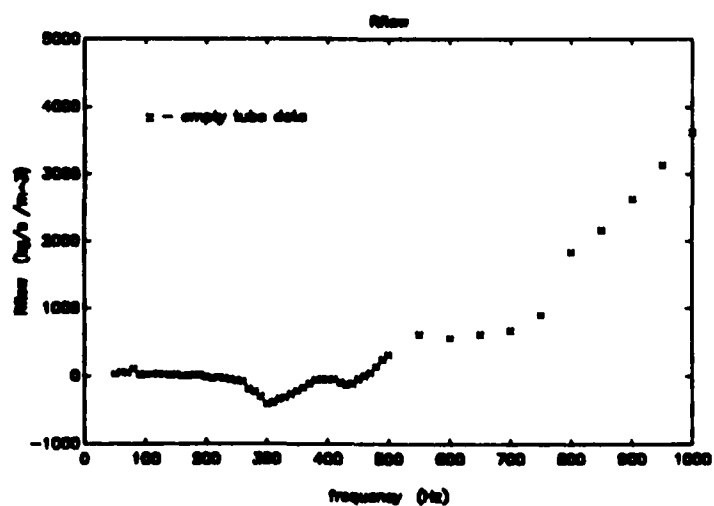


Figure 20 Revised empty tube results - flow resistance.

It is apparent from the results shown in Figure 19 that the objective of this experiment was achieved, namely, to test the apparatus and equipment setup on a known quantity, i.e. air in an empty sample tube.

At this point the interpretation of the results for flow resistance shown in Figure 20 are not of a major concern, since flow resistance is not really a relevant quantity for air in an empty tube. In addition, a thorough discussion of flow resistance requires the introduction of concepts, such as viscous penetration depth, which are much more relevant to air in a porous solid. Therefore, these concepts will be introduced in the next chapter and a complete discussion of flow resistance will follow. The results of both empty tube and porous solid experiments will be included in that discussion.

V. POROUS SOLID SAMPLE EXPERIMENTS

A. POROUS SOLID SAMPLE SELECTION

The measure of the influence of fluid shear viscosity on a fluid saturated porous solid subject to elastic wave propagation is the viscous penetration depth, defined as:

$$\delta_{visc} = \left[\frac{2\eta}{\omega \rho} \right]^{1/2}, \quad (5.1)$$

where ρ is the fluid mass density, η is the fluid shear viscosity, and ω is the frequency. The ratio of viscous penetration depth to a characteristic pore size is one of the most fundamental dimensionless parameters that determines the nature of elastic wave propagation in a fluid saturated porous solid (Baker, 1986, p. 27).

If the viscous penetration depth is much less than a characteristic pore size, then the motion of the fluid is very similar to that of an inviscid fluid, and independent (of the solid) sound propagation within the fluid is possible. In the porous solid literature this case is referred to as the high frequency or boundary layer flow limit.

If the viscous penetration depth is much greater than a characteristic pore size, then the fluid in the pores is essentially frozen to the solid and sound cannot propagate within the fluid. This case is referred to as the low frequency or Poiseuille flow limit.

Both cases are of interest and were investigated. The measure of characteristic pore size used was mean pore diameter since this was the

only measure the porous solid sample manufacturer (General Polymeric, West Reading, PA.) could work with. Three samples with mean pore diameters of 150, 300, and 500 microns were selected so that over the frequency band of interest, 50 to 1000 Hz, both types of flow could be observed and the transition between the two types of flow would occur at several different frequencies.

Figure 20 shows the estimated transition from Poiseuille flow to boundary layer flow (plug flow) for a 300 micron sample.

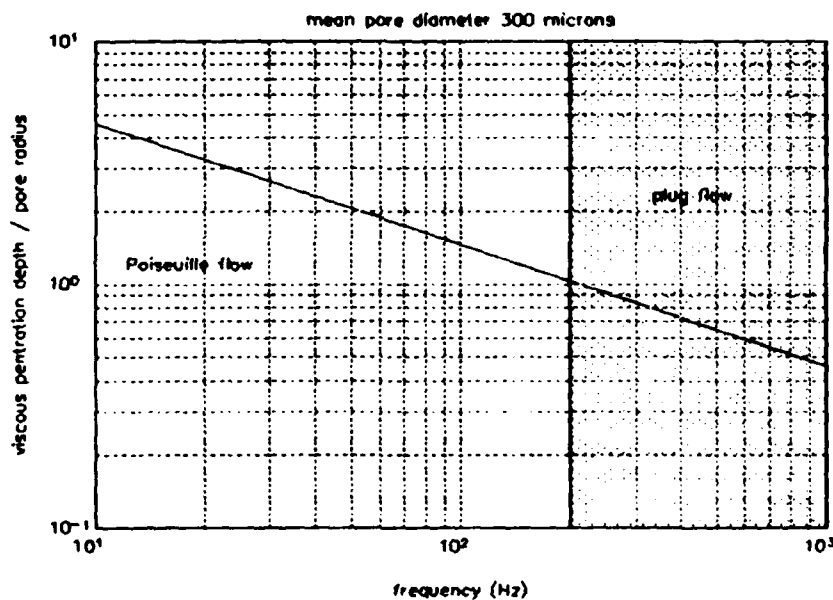


Figure 20 Estimated flow transition for a 300 micron sample.

B. THEORY

The procedure developed for the revised empty tube experiment was used since it avoids corrections for the acceleration loss due to the compressibility of the air between the speakers and the ends of the

sample. The empty sample tube was, however, replaced with a sample tube containing a porous solid sample as shown in Figure 21.

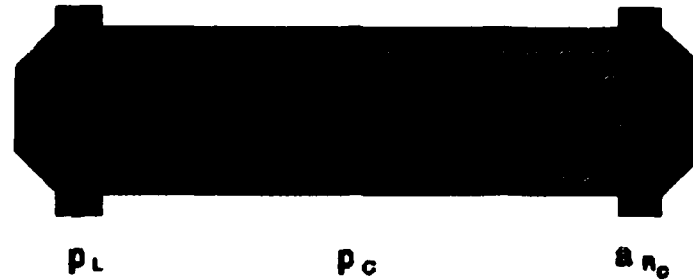


Figure 21 Porous solid sample experimental setup.

The slave HP 3314 was again adjusted to obtain a null in pressure at right end of the sample tube. Therefore, the complex effective mass density of the air contained in the sample can be computed using

$$\bar{p}_w = - \frac{\bar{\nabla p}}{a_R \cdot acf} \cdot \frac{1}{fwcf} , \quad (5.2)$$

where

$$\bar{\nabla p} = - \frac{p_L}{L} , \quad (5.3)$$

$$fwcf = \left[\frac{\sin kL}{kL} \right] , \quad (5.4)$$

and a_R is the acceleration of the right speaker cone. The acceleration correction factor, acf , used for the empty tube experiments; however, needs to be modified.

1. Modified Acceleration Correction Factor

The method used to develop the acceleration correction factor for the empty tube experiments can again be used; however, this time the mass flow rate of the air at the surface of the speaker cone and the mass flow rate of air at the end of the sample tube are related as follows:

$$a_{cone} A_{cone} = a_{sample} A_{sample} P_{sample} \quad (5.5)$$

where

a_{cone} = acceleration of the surface of the speaker cone,

a_{sample} = acceleration of the air at the end of the sample,

A_{cone} = cross-sectional area of the speaker cone,

A_{sample} = cross-sectional area of the end of the sample,

P_{sample} = porosity of the sample.

The additional parameter, P_{sample} , the porosity of the sample, is defined as the ratio of the volume occupied by the fluid to the total sample volume. It is required since the cross-sectional area of the fluid is reduced by the frame of the porous material.

Solving Equation (5.5) for the desired quantity, a_{sample} yields:

$$a_{sample} = a_{cone} \frac{1}{P} \frac{A_{cone}}{A_{sample}} = a_{cone} \frac{1}{P} \left[\frac{D_{cone}}{D_{sample}} \right]^2 \quad (5.6)$$

where

D_{cone} = diameter of the speaker cone (8.3 cm.),

D_{sample} = diameter of the sample (8.9 cm.).

Hence,

$$acf = \frac{1}{P} \left[\frac{D_{core}}{D_{sample}} \right]^2 = \frac{1}{P} 0.870 \quad (5.7)$$

is the modified acceleration correction factor. The acceleration correction factor used for the empty tube experiments, Equation (4.20), can be obtained from Equation (5.7) by setting the porosity equal to one.

a. Porosity Measurements

The porous solid samples were constructed of glass spheres with a density, ρ , of 2.4 g/cm³ bonded together to form a slug that was pressed inside of an empty sample tube. The porosity of each sample was determined by comparing the expected mass of a solid glass sample of identical size, constructed with glass of the same density, and the actual mass of the porous sample.

The expected mass of a solid glass sample is

$$\rho \cdot volume = \rho \cdot \frac{\pi}{4} d^2 h \quad (5.8)$$

where

d = diameter of the sample (8.89 cm),

h = height (length) of the sample (10.38 cm).

Hence, the expected mass of a solid glass sample is 1546 g.

The porosity of a given sample is a function of the ratio of the actual mass of the porous solid sample to the expected mass of a solid glass sample, that is

$$P = 1 - \frac{\text{actual mass}}{\text{expected mass}} \quad (5.9)$$

The results of the porosity measurements are summarized in Table 5.1.

Table 5.1 POROSITY MEASUREMENTS

sample	mean pore dia (microns)	mass (g)	ratio	porosity P
1	150	1002.3	0.65	0.35
2	300	985.6	0.64	0.36
3	500	973.5	0.63	0.37

2. Estimating kL in a Rigid Porous Solid.

For the empty tube experiments, the wave number is the same as for free space, $k = \frac{\omega}{c}$ with $c \approx 340$ m/s. However, for these experiments the tube was filled with a rigid porous solid, and the speed of the pressure wave was not known *a priori*. Therefore, a method had to be developed to determine the wave number.

The method chosen was to calculate the wave number based on pressure measurements taken at the left end and the center of the sample tube as follows:

The pressure at the left end of the sample is

$$p_L = p(-L) = -p_0 \sin k(-L) = p_0 \sin kL, \quad (5.10)$$

which can be written as

$$p_L = 2p_0 \sin \left[\frac{kL}{2} \right] \cos \left[\frac{kL}{2} \right], \quad (5.11)$$

and the pressure at the center of the sample, p_C , is

$$p_C = p\left(-\frac{L}{2}\right) = -p_0 \sin k\left[-\frac{L}{2}\right] = p_0 \sin \left[\frac{kL}{2} \right]. \quad (5.12)$$

Then taking the ratio of the two pressures,

$$\frac{p_L}{p_C} = 2 \cos \left[\frac{kL}{2} \right]. \quad (5.13)$$

Solving Equation (5.13) for kL in terms of the two pressures then gives

$$kL = \frac{1}{2} \cos^{-1} \left[\frac{p_L}{p_C} \right]. \quad (5.14)$$

This estimate was used in Equation (5.4) for the finite wavelength correction factor, f_{wcf} .

C. RESULTS

Measurements for each of the samples were made over the frequency range of 50 to 500 Hz in 10 Hz steps and over the frequency range of 500 to 1000 Hz in 50 Hz steps. The amplitude and phase of the slave HP 3314 was adjusted at each step to obtain a null in pressure at the right end of the sample tube. Once the null was obtained, pressure and acceleration

measurements (both amplitude and phase) were taken using the SR Lock-in Amplifier, pressure at the center and the left end of the sample tube, acceleration at the right end of the sample tube (speaker cone).

A computer program was written to compute the complex effective mass density of the air contained in the sample at each frequency using Equation (5.2). Then, since

$$\tilde{\rho}_{eff} = \rho_{eff} - j \frac{R_{flow}}{\omega}, \quad (5.15)$$

the effective fluid mass density of the air contained in the sample is

$$\rho_{eff} = \text{Re}[\tilde{\rho}], \quad (5.16)$$

and the flow resistance is

$$R_{flow} = -\omega \text{Im}[\tilde{\rho}]. \quad (5.17)$$

A copy of the program is attached as Appendix C.

Plots of the effective mass density and flow resistance of the air contained in the 150 micron sample are shown in Figures 22 and 23 respectively. Similar plots for the 300 micron and 500 micron samples are shown in Figures 24 through 27. Included on each plot of the effective mass density for reference is the effective mass density of air contained in an empty sample tube at 20° C.

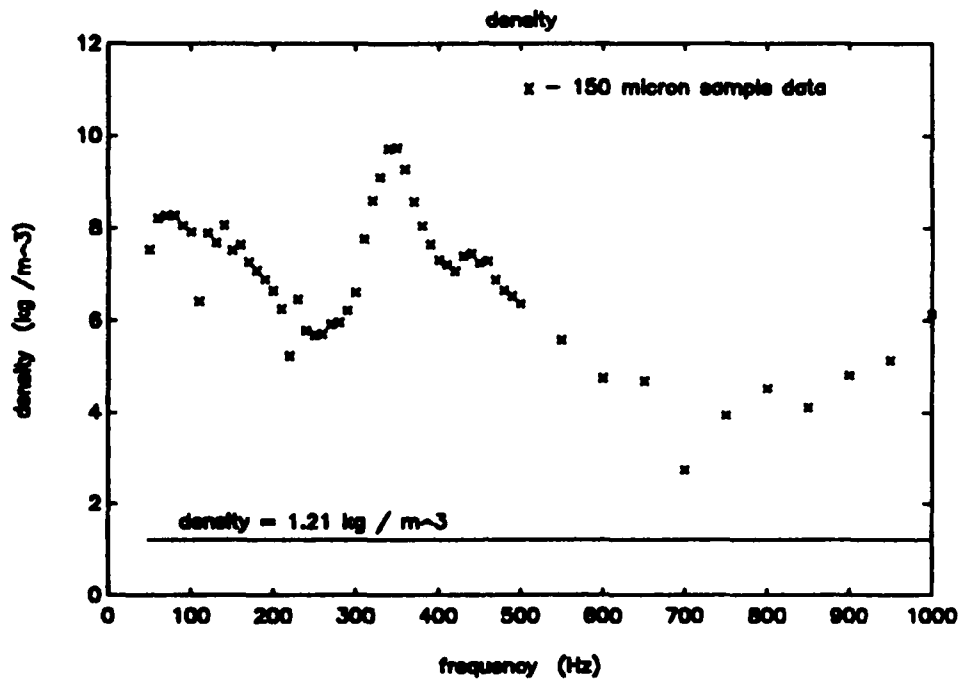


Figure 22 Effective mass density - 150 micron sample.

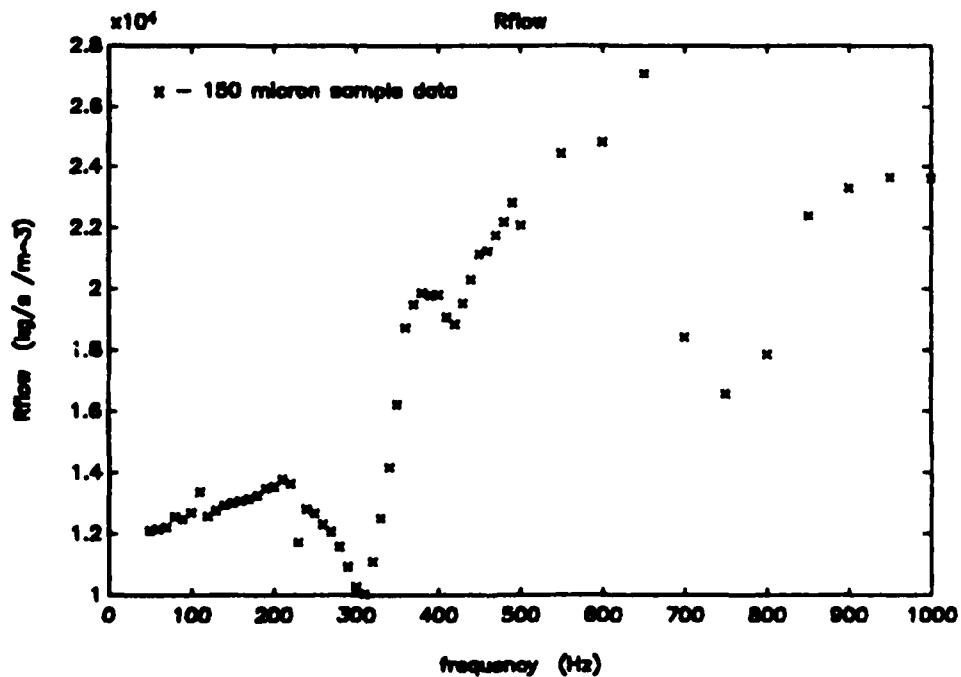


Figure 23 Flow resistance - 150 micron sample.

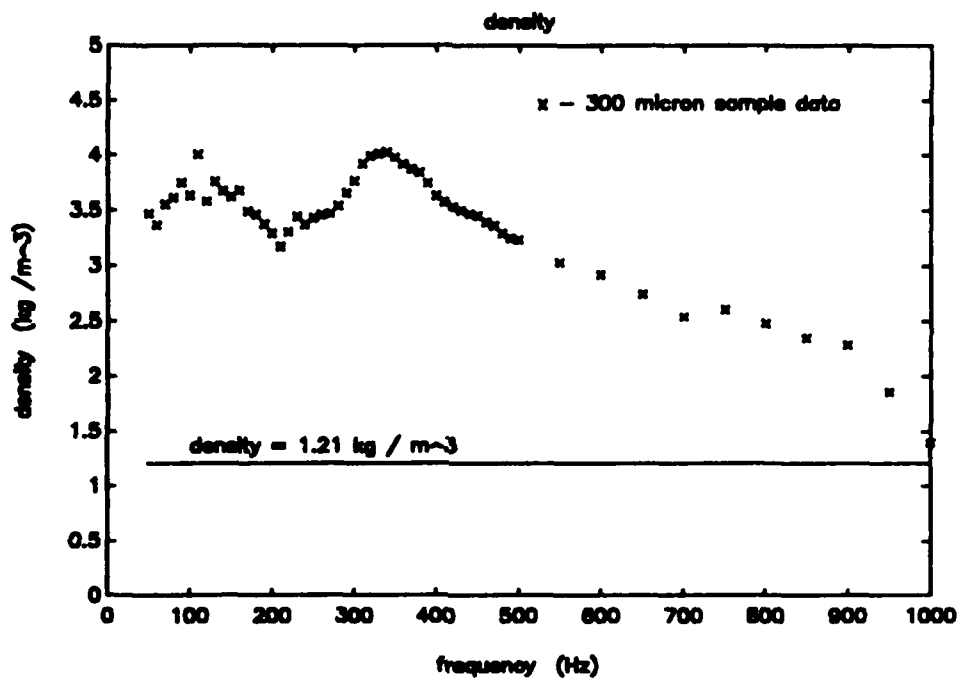


Figure 24 Effective mass density - 300 micron sample.

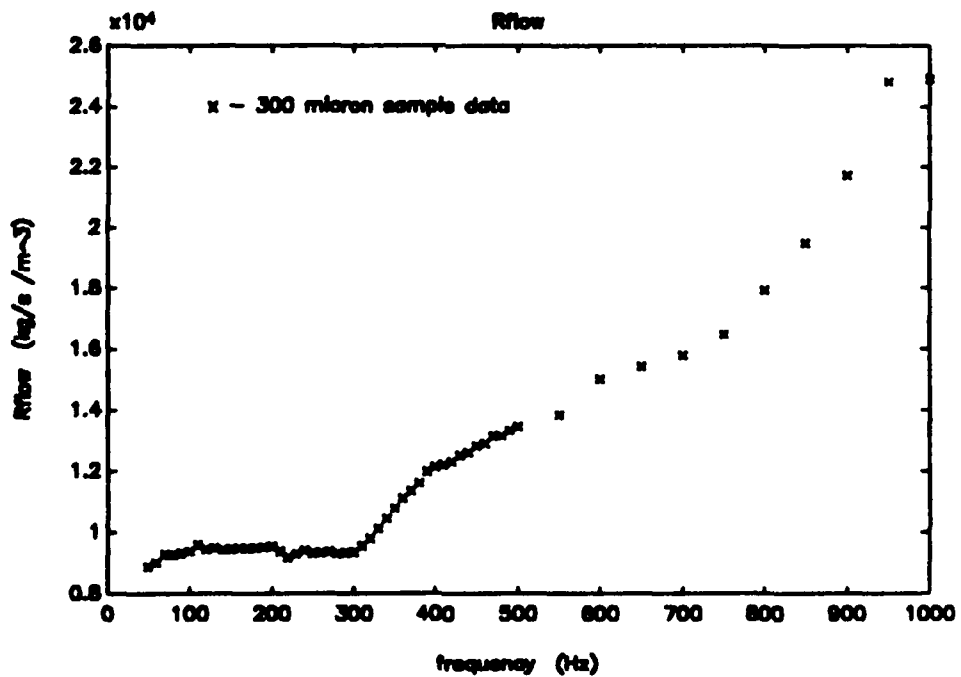


Figure 25 Flow resistance - 300 micron sample.

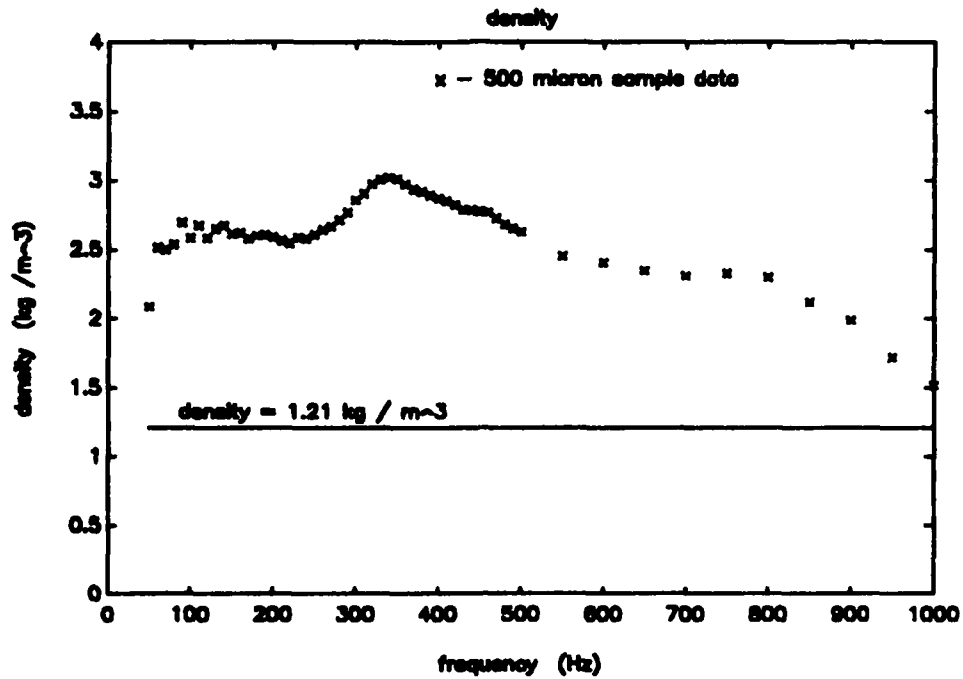


Figure 26 Effective mass density - 500 micron sample.

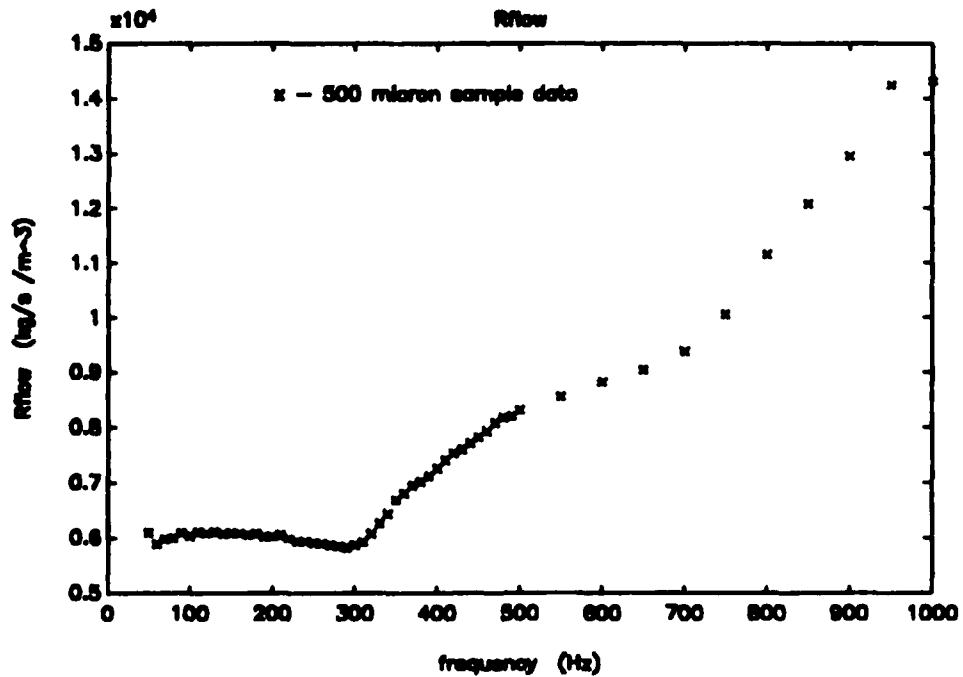


Figure 27 Flow resistance - 500 micron sample.

D. INTERPRETATION OF RESULTS

1. Calculation of $\tilde{\rho}_{eff}$ using Biot's Theory

Using Biot's theory, the complex effective mass density can be expressed as follows (Baker, 1986, pp. 44, 48):

$$\tilde{\rho}_{eff} = \tilde{\alpha}(\omega) \rho_f = \alpha \rho_f + \frac{R_{DC}}{j\omega} \tilde{F}(\kappa), \quad (5.18)$$

where α is the (intrinsic) tortuosity, ρ_f is the mass density of the bulk fluid, R_{DC} is the DC flow resistance, and $\tilde{F}(\kappa)$ is Biot's universal complex, frequency dependent correction function, whose purpose is to make the frequency dependence of $\tilde{\rho}_{eff}$ come out right. $\tilde{F}(\kappa)$ is defined by (Baker, 1986, p. 53)

$$\tilde{F}(\kappa) = \frac{z J_1(z)}{4 J_2(z)}, \quad (5.19)$$

where

$$z = j^{\frac{3}{2}}(\kappa) \quad \text{and} \quad \kappa = \delta \left[\frac{R_{DC}}{\alpha \omega \rho_f} \right]^{-\frac{1}{2}}, \quad (5.20)$$

and δ is the Biot "structural factor", a dimensionless parameter which depends only upon pore shape. The three parameters α , R_{DC} , and δ completely characterize the microscopic pore geometry in Biot's theory.

Although the tortuosity α may be obtained experimentally, it is found to depend primarily on the porosity P in a nearly predictably fashion which for the case of a porous solid constructed of a random

collection of spheres is adequately represented by (Sen et. al. 1981, Johnson and Sen 1981)

$$\alpha = P^{-1/2} \quad (5.21)$$

Calculations of tortuosity for each of the samples using Equation (5.21) are summarized in Table 5.2.

Table 5.2 TORTUOSITY CALCULATIONS

sample	mean pore dia (microns)	porosity P	tortuosity α
1	150	0.35	1.69
2	300	0.36	1.67
3	500	0.37	1.64

The structural factor δ depends weakly upon the cross-sectional shape of the pores. Baker suggests a value of 4 for δ for a porous solid constructed of a random collection of spheres (Baker, 1986, pp. 291 -292).

The DC flow resistance is proportional to the square of the ratio of the viscous penetration depth to a characteristic pore size (Baker, 1986, p. 45). Hence,

$$R_{DC} \sim \frac{\eta}{(\text{pore size})^2} \quad (5.22)$$

where η is the fluid shear viscosity. Therefore, the low frequency limit of the flow resistance should decrease with increasing pore diameter. This is clearly the case as shown in Figure 28.

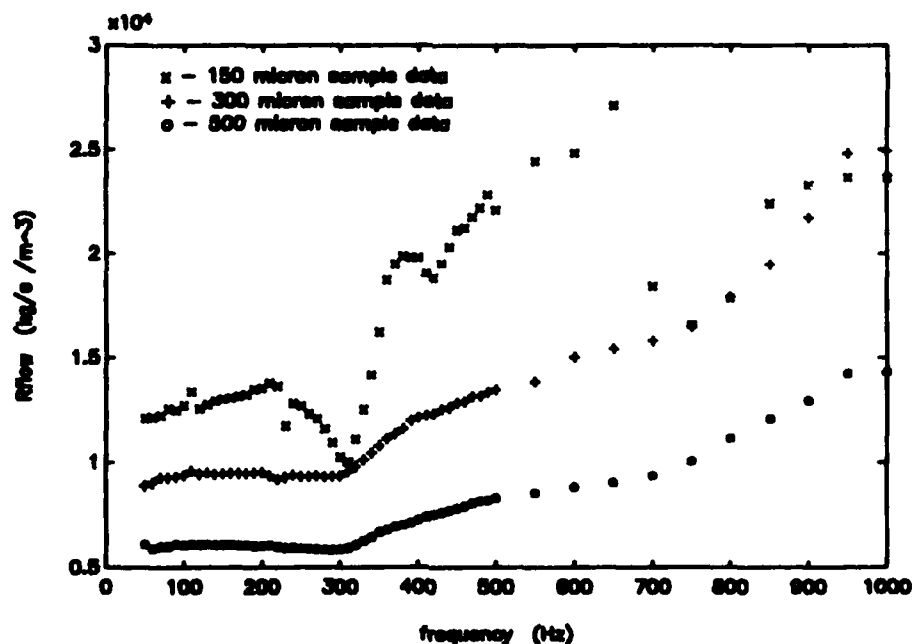


Figure 28 Flow resistance - 150, 300, and 500 micron samples.

Hence, it was decided that the DC flow resistance for each sample could be obtained from a least squares fit of the low frequency portion of the flow resistance results, as shown in Figures 23, 25, and 27, for that sample. The results are summarized in Table 5.3.

Table 5.3 DC Flow Resistance

sample	mean pore dia (microns)	DC flow resistance ($\times 10^4$ kg/s/m ²)
1	150	1.25
2	300	0.94
3	500	0.60

Therefore, theoretical values of the complex effective mass density can be calculated using Equation (5.18) for each of the porous solid samples. However, the quantities of interest are the effective fluid mass density and the flow resistance.

2. Effective Fluid Mass Density

The (real) effective fluid mass density, $\rho_{eff}(\omega)$, is found from $\tilde{\rho}_{eff}$ (Equation 5.18), by

$$\rho_{eff}(\omega) = \text{Re}[\tilde{\rho}_{eff}] = \alpha \rho_f + \frac{R_{DC}}{\omega} \text{Im}[\tilde{F}(\kappa)] . \quad (5.23)$$

A plot of the effective mass density of the air contained in the 150 micron sample and its theoretical effective mass density calculated using Equation (5.23) is shown in Figure 29. Similar plots for the 300 micron and 500 micron samples are shown in Figures 30 and 31, respectively.

Although the experimental results for the 150 and 500 micron samples do not entirely agree with their theoretical results, there is good agreement between the experimental and theoretical results for the 300 micron sample.

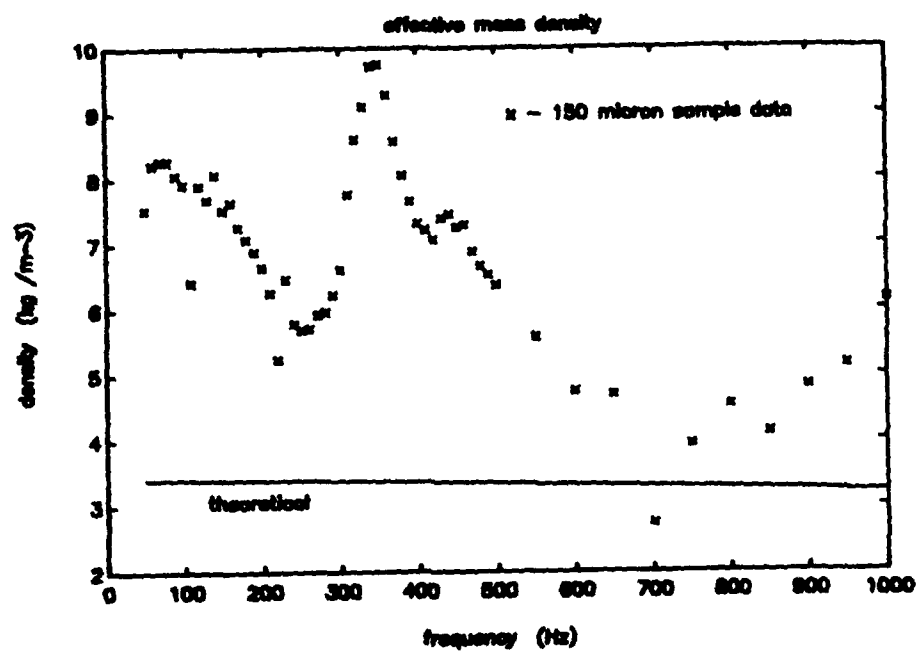


Figure 29 Effective mass density - 150 micron sample.

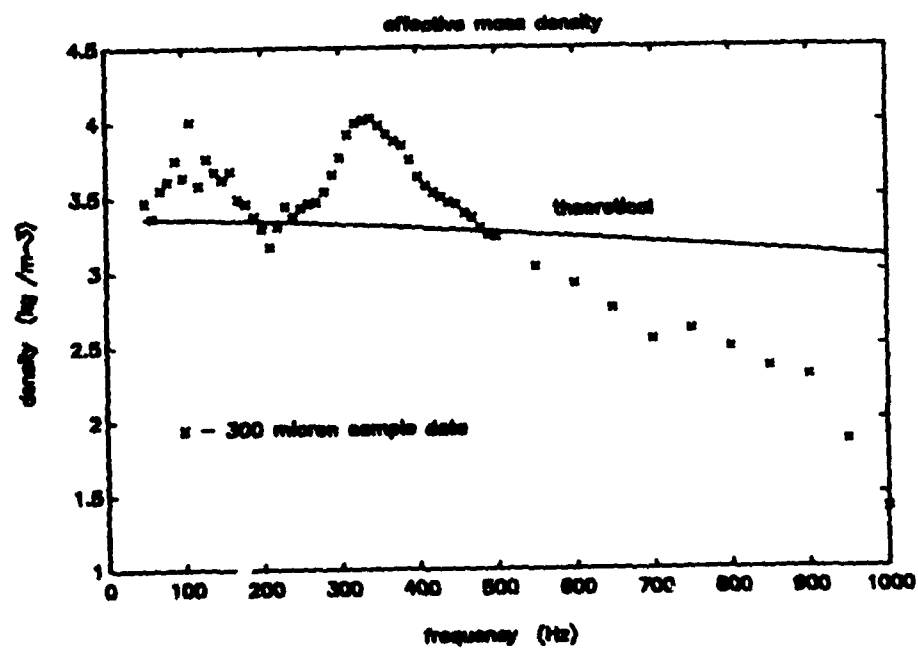


Figure 30 Effective mass density - 300 micron sample.

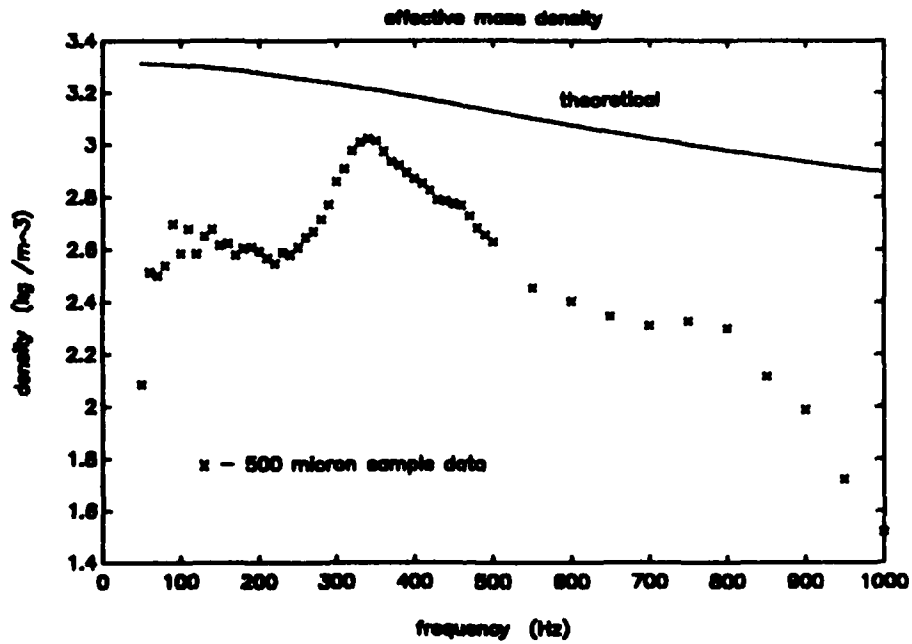


Figure 31 Effective mass density - 500 micron sample.

3. Flow Resistance

The frequency dependent flow resistance, $R_{flow}(\omega)$, is found from $\tilde{\rho}_{eff}$ (Equation 5.18), by

$$R_{flow}(\omega) = -\omega \text{Im}[\tilde{\rho}_{eff}] = R_{DC} \text{Re}[\tilde{F}(\kappa)] . \quad (5.24)$$

A plot of the flow resistance of the air contained in the 150 micron sample and its theoretical flow resistance calculated using Equation (5.24) is shown in Figure 32. Similar plots for the 300 micron and 500 micron samples are shown in Figures 33 and 34, respectively.

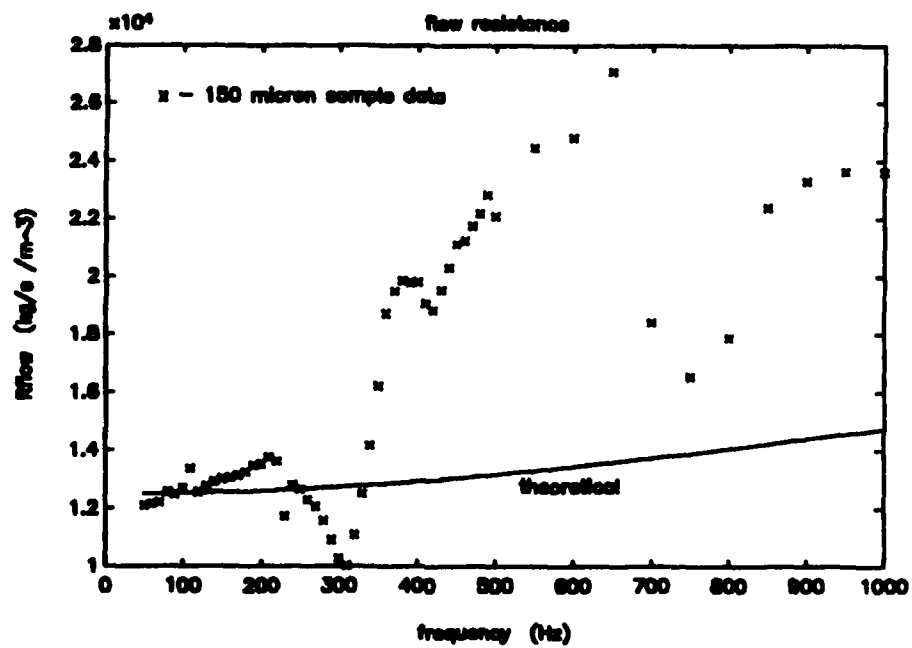


Figure 32 Flow resistance - 150 micron sample.

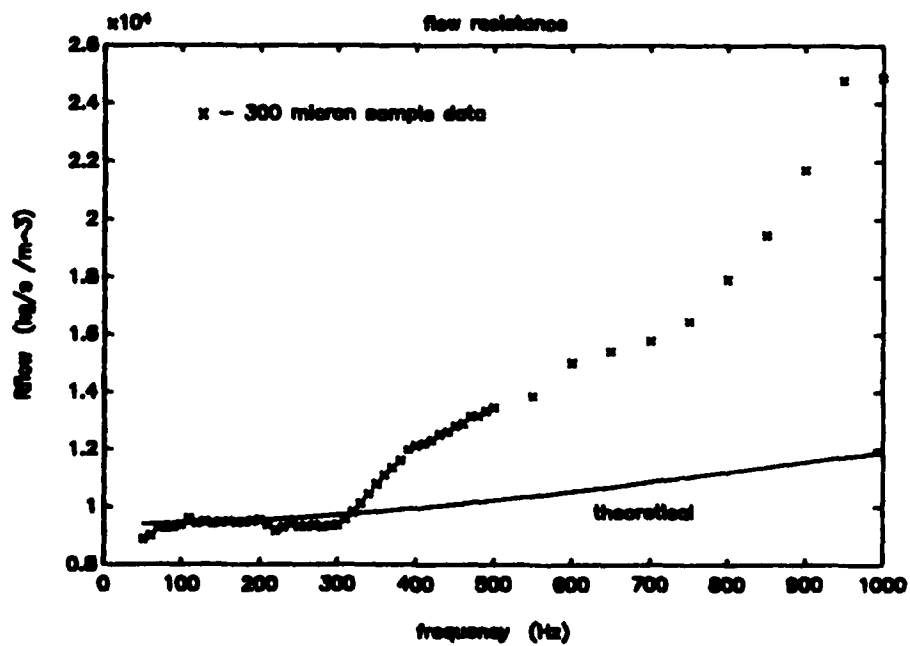


Figure 33 Flow resistance - 300 micron sample.

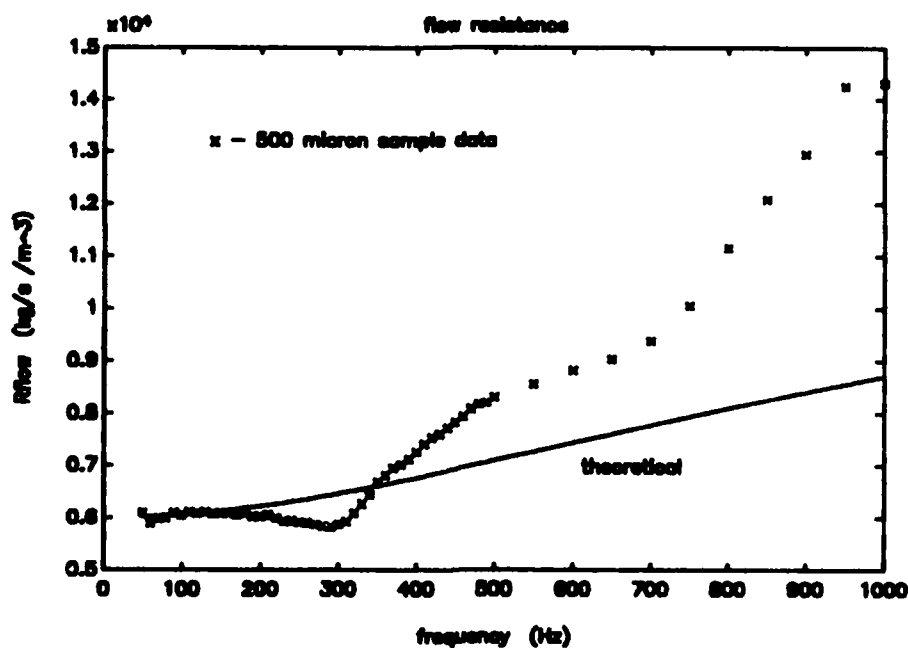


Figure 34 Flow resistance - 500 micron sample.

Although the experimental results do not entirely agree with the theoretical results, especially at the high frequency limit, they do show a similar trend. Baker points out that the high frequency limit of flow resistance should be proportional to $\omega^{\frac{1}{2}}$ and that the low frequency limit of flow resistance should be proportional to ω^0 . This is clearly the case, as shown in Figure 35. The log scale was chosen since it makes the calculated limits appear as straight lines and thus makes the comparison easier to visualize.

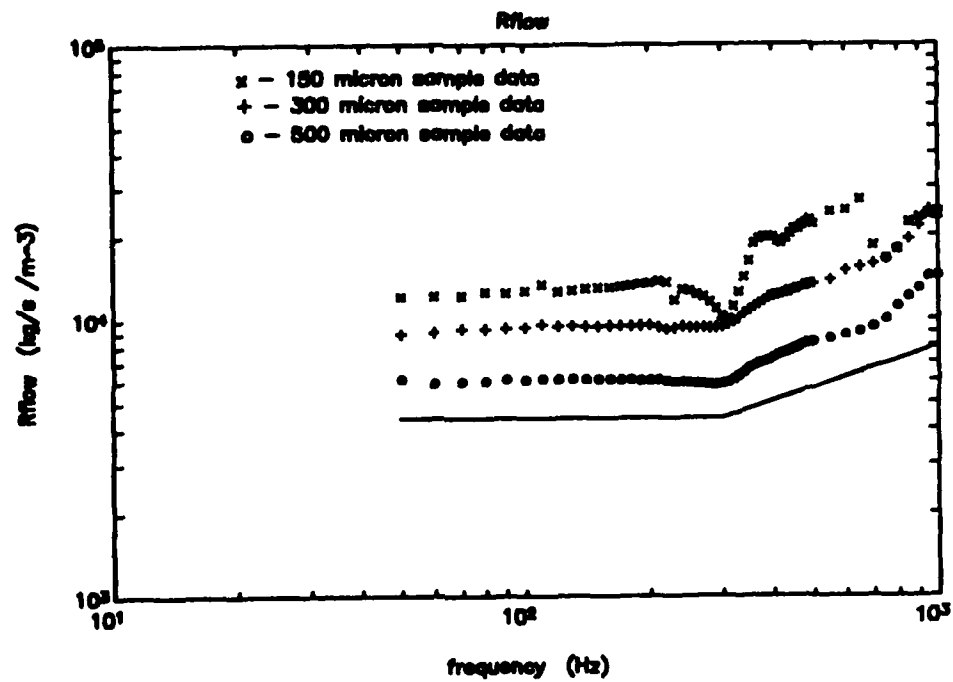


Figure 35 Flow resistance - 150, 300, and 500 micron samples.

VI. CONCLUSIONS AND RECOMMENDATIONS

An experimental apparatus was designed and built to obtain the effective mass density and flow resistance of air in a porous solid from acoustic pressure and acceleration measurements.

Initial experiments were conducted to test the apparatus and equipment setup on a known quantity, namely air in an empty sample tube. The objective of these experiments was substantially achieved after minor modifications to the apparatus and a revision to the experimental procedure were made.

Porous solid sample experiments were conducted using three samples with mean pore diameters of 150, 300, and 500 microns. The results of these experiments were encouraging, especially for the 300 and 500 micron samples. However, the flow resistance results had a much closer agreement with theory than the effective mass density results. All results were repeatable and consistent from sample to sample.

Future research should focus on the 300 and 500 micron samples since they produced the best results. Areas of interest include the possible transition between Poiseuille flow and boundary layer flow at 300 Hz vice the predicted frequencies, and the corrections required to make the theory fit the data.

APPENDIX A PROGRAM FOR INITIAL EMPTY TUBE CALCULATIONS

```

% initial empty tube calculations

%-----
%   environmental and equipment parameters
%-----

%   gravity, m/s/s
%   g = 9.8;

%   speed of sound in air, m/s
%   c = 343;

%   frequency
%   freq = [50:10:490,500:50:1000];
%   omega = 2*pi*freq;

%   wave number
%   k = omega / c;

%   accelerometer sensitivities, mV/g
%   lasen = - 4.75;
%   rasen = - 4.56;

%   pressure sensor sensitivities, mV/Pa
%   right
%   rpsen = 10^((16.13 - 0.0015 * freq) / 20);
%   rpsen = - rpsen;

%   left
%   lpsen = 10^((15.53 - 0.00035 * freq) / 20);
%   lpsen = - lpsen;

%   Note: negative sensitivities due to reverse polarity of
%   both accelerometers and pressure sensors

%-----
%   empty tube parameters
%-----

%   length of sample tube, m
%   l = .102;

```

```

%-----
%               empty tube data in mVolts
%-----

load emty.dat
lpv = emty(1:56,1) + j*emty(1:56,2);
rpv = emty(57:112,1) + j*emty(57:112,2);
lav = emty(113:168,1) + j*emty(113:168,2);
rav = emty(169:224,1) + j*emty(169:224,2);

%-----
%               conversions to Pa and m/s/s
%-----

% pressure
rp = rpv ./ rpsen.';
lp = lpv ./ lpsen.';

% acceleration
la = lav / (lasen/g);
ra = rav / (rasen/g);
ra = - ra;

% Note: the accelerometers mounted to the surface
% of the speaker cones were calibrated such that
% the direction of positive acceleration is outward

%-----
%               correction factors
%-----

% acceleration correction factor
acf = (8.3 / 8.9)^2;

% finite wavelength correction factor
fwcf = tan(k*l/2) ./ (k*l/2);

%-----
%               final calculations
%-----

delta_p = rp - lp;
grad_p = delta_p / l;

accel = (la + ra) / 2;
accel = accel * acf;

result = - (grad_p ./ accel) ./ fwcf';
density = real(result);
Rflow = - omega' .* imag(result);

```

APPENDIX B PROGRAM FOR REVISED EMPTY TUBE CALCULATIONS

```
% revised empty tube calculations

%-----
%   environmental and equipment parameters
%-----

%   gravity, m/s/s
%   g = 9.8;

%   speed of sound in air, m/s
%   c = 343;

%   frequency
%   freq = [50:10:490,500:50:1000];
%   omega = 2*pi*freq;

%   wave number
%   k = omega / c;

%   accelerometer sensitivity, mV/g
%   rasen = - 4.56;

% Note: negative sensitivity due to reverse polarity
%       of accelerometer

%   pressure sensor sensitivity, mV/Pa
%   lpsen = 0.3017;

%-----
%   empty tube parameters
%-----

%   effective length of sample tube, m
%   l = .092;

%-----
%   empty tube data in mVolts
%-----

load empty.dat
lpv = empty(1:56,1) + j*empty(1:56,2);
rav = empty(113:168,1) + j*empty(113:168,2);
```

```

%-----
%      conversions to Pa and m/s/s
%-----

%  pressure
    lp = lpv / lpsen;

%  acceleration
    ra = rav / (rasen/g);
    ra = -ra;

%  Note: the accelerometer mounted to the surface
%  of the speaker cone was calibrated such that
%  the direction of positive acceleration is outward

%-----
%      correction factors
%-----

%  acceleration correction factor
    acf = (8.3 / 8.9)^2;

%  finite wavelength correction factor
    fwcf = sin(k*l) ./ (k*l);

%-----
%      final calculations
%-----

    delta_p = - lp;
    grad_p = delta_p / l;

    accel = ra;
    accel = accel * acf;

    result = - (grad_p ./ accel) ./ fwcf';
    density = real(result);
    Rflow = - omega' .* imag(result);

```


APPENDIX C PROGRAM FOR POROUS SOLID SAMPLE CALCULATIONS

```
% porous solid sample calculations

%-----
%   environmental and equipment parameters
%-----

%   gravity, m/s/s
%   g = 9.8;

%   frequency
%   freq = [50:10:490,500:50:1000];
%   omega = 2*pi*freq;

%   accelerometer sensitivity, mV/g
%   rasen = - 4.56;

% Note: negative sensitivity due to reverse polarity
%       of accelerometer

%   pressure sensor sensitivities, mV/Pa
%   lpsen = 0.3017;
%   cpsen = 0.2775;

%-----
%               sample data in mVolts
%-----

load sample15.dat
lpv = sample15(1:56,1) + j*sample15(1:56,2);
cpv = sample15(57:112,1) + j*sample15(57:112,2);
rav = sample15(113:168,1) + j*sample15(113:168,2);

%-----
%               sample parameters
%-----

%   effective length of the sample, m
%   l = .092;

%   porosity of sample
%   P = 0.37;
```

```

%-----
%               conversions to Pa and m/s/s
%-----

%   pressure
    lp = lpv / lpsen;
    cp = cpv / cpsen;

% acceleration
    ra = rav / (rasen/g);
    ra = - ra;

% Note: the accelerometer mounted to the surface
% of the speaker cone was calibrated such that
% the direction of positive acceleration is outward

%-----
%               correction factors
%-----

% acceleration correction factor
    acf = (1/P) * (8.3 / 8.9)^2;

% finite wavelength correction factor
    kl  = 2 * acos( lp ./ (2 * cp) );
    fwcf = sin(kl) ./ (kl);

%-----
%               final calculations
%-----

    delta_p = - lp;
    grad_p  = delta_p / l;

    accel = ra;
    accel = accel * acf;

    result = - (grad_p ./ accel) ./ fwcf;
    density = real(result);
    Rflow   = - omega' .* imag(result);

```

LIST OF REFERENCES

Baker, S. R., *Sound Propagation in a Superfluid Helium Filled Porous Solid: Theory and Experiment*, PhD Dissertation, Department of Physics, University of California at Los Angeles, July 1986.

Johnson, D. L., and Sen, P. N., "Multiple Scattering of Acoustic Waves with Application to the Index of Refraction of Fourth Sound", *Phys. Rev* v. 24, p. 2486, 1981

Kinsler, L. E., Frey, A. R., Coppens, A. B., and Sanders, J. V., *Fundamentals of Acoustics*, John Wiley & Sons, Inc., 1982

Sen, P. N., Scala, C., and Cohen, M. H., "A Self-Similar Model for Sedimentary Rocks with Application to the Dielectric Constant of Fused Glass Beads", *Geophysics*, v. 46, p. 781, 1981

Urlick, R. J., *Principles of Underwater Sound*, Mc Graw Hill, Inc., 1983.

INITIAL DISTRIBUTION LIST

- | | | |
|----|--|---|
| 1. | Defense Technical Information Center
Cameron Station
Alexandria, VA 22304-6145 | 2 |
| 2. | Library, Code 0052
Naval Postgraduate School
Monterey, CA 93943-5000 | 2 |
| 3. | Professor S. R. Baker (Code PH/Ba)
Naval Postgraduate School
Monterey, CA 93943-5000 | 8 |
| 4. | Professor A. A. Atchley (Code PH/Ay)
Naval Postgraduate School
Monterey, CA 93943-5000 | 1 |
| 5. | LT Kevin A. Grundy, USN
5513 Bittern Ave.
Ewa Beach, HI 96706-3226 | 2 |